Cytoskeletal confinement of CX$_3$CL1 limits its susceptibility to proteolytic cleavage by ADAM10

Harikesh S. Wong[a,b], Valentin Jaumouillé[a], Bryan Heit[c], Sasha A. Doodnauth[a], Sajedabanu Patel[a], Yi-Wei Huang[a], Sergio Grinstein[a,d], and Lisa A. Robinson[a,b,e]

[a]Program in Cell Biology, Hospital for Sick Children, Toronto, ON M5G 1X8, Canada; [b]Institute of Medical Science, University of Toronto, Toronto, ON M5S 1A8, Canada; [c]Department of Microbiology and Immunology, University of Western Ontario, London, ON N6A 5C1, Canada; [d]Keenan Research Centre of the Li Ka Shing Knowledge Institute, St. Michael's Hospital, Toronto, ON M5B 1W8, Canada; [e]Department of Paediatrics, University of Toronto, Toronto, ON M5S 2J7, Canada

ABSTRACT CX$_3$CL1 is a unique chemokine that acts both as a transmembrane endothelial adhesion molecule and, upon proteolytic cleavage, a soluble chemoattractant for circulating leukocytes. The constitutive release of soluble CX$_3$CL1 requires the interaction of its transmembrane species with the integral membrane metalloprotease ADAM10, yet the mechanisms governing this process remain elusive. Using single-particle tracking and subdiffraction imaging, we studied how ADAM10 interacts with CX$_3$CL1. We observed that the majority of cell surface CX$_3$CL1 diffused within restricted confinement regions structured by the cortical actin cytoskeleton. These confinement regions sequestered CX$_3$CL1 from ADAM10, precluding their association. Disruption of the actin cytoskeleton reduced CX$_3$CL1 confinement and increased CX$_3$CL1–ADAM10 interactions, promoting the release of soluble chemokine. Our results demonstrate a novel role for the cytoskeleton in limiting membrane protein proteolysis, thereby regulating both cell surface levels and the release of soluble ligand.

INTRODUCTION

The recruitment of leukocytes to sites of inflammation involves a complex series of coordinated signaling cascades mediating interactions between leukocytes and the injured endothelium. Two critical components of this process are chemokines, responsible for attraction and activation of leukocytes, and endothelial adhesion molecules, responsible for firm adhesion of leukocytes to endothelial cells (ECs; Huang *et al.*, 2009). Among the >40 chemokines described, CX$_3$CL1, also known as fractalkine, is one of only two that

can exist both as a soluble chemokine and a transmembrane, endothelial adhesion molecule (Bazan *et al.*, 1997; Fong *et al.*, 1998, 2000; Imai *et al.*, 1997). Of importance, CX$_3$CL1 binds only one known receptor, CX$_3$CR1, expressed by various leukocytes, including monocytes, subpopulations of T lymphocytes, and natural killer (NK) cells (Fong *et al.*, 1998). In recent years, CX$_3$CL1 and its receptor have been implicated in the pathogenesis and progression of many inflammatory disorders, including organ transplant rejection, renal inflammation, rheumatoid arthritis, and, most notably, atherosclerosis (Robinson *et al.*, 2000; Haskell *et al.*, 2001; Ruth *et al.*, 2001; Combadiere *et al.*, 2003; Lesnik *et al.*, 2003; Lucas *et al.*, 2003; Nakatani *et al.*, 2010).

Conversion of CX$_3$CL1 from the transmembrane to the soluble species occurs through proteolytic cleavage that can be mediated by two metalloproteases: a disintegrin and metalloproteinase domain–containing protein 10 (ADAM10), a constitutively active protease, and the tumor necrosis factor-α–converting enzyme (TACE, also called ADAM17), a protease with inducible activity (Garton *et al.*, 2001; Tsou *et al.*, 2001; Hundhausen *et al.*, 2003). The mechanisms controlling these processes, however, have not been well defined. Whereas TACE remains inactive in the absence of stimulation, ADAM10 is constitutively active, yet, paradoxically, cleaves

only a small fraction of CX_3CL1 in the basal state (Hundhausen *et al.*, 2003). Thus it is conceivable that either ADAM10 has limited proteolytic activity or is physically restricted from accessing the entire pool of cell surface CX_3CL1.

Molecules in the plasma membrane can be compartmentalized by the cytoskeleton or segregated into lipid microdomains, which restrict and regulate their lateral diffusion (Kusumi *et al.*, 2005a,b; Suzuki *et al.*, 2007; Andrews *et al.*, 2008; Goswami *et al.*, 2008; Treanor *et al.*, 2010, 2011). Whether membrane compartmentalization can regulate proteolysis by limiting protease–substrate interactions has not been explored. To address these questions, we used a combination of single-particle tracking, immunochemistry, and subdiffraction imaging to study both CX_3CL1 and ADAM10. Our results indicate that cortical actin confinement regions restrict plasmalemmal CX_3CL1 mobility. We further demonstrate that this confinement limits interactions between ADAM10 and CX_3CL1, regulating the amount of transmembrane chemokine cleaved by the protease. Taken together, our results reveal an unprecedented regulatory role of the cytoskeleton in protecting substrates from proteolytic cleavage, thereby controlling the availability of ligand on the plasma membrane, as well as the release of ligand from the plasma membrane.

RESULTS

CX_3CL1 experiences confined motion on the surface of endothelial cells

To investigate the dynamics of CX_3CL1 in living cells, we assessed the mobility of individual molecules using single-particle tracking (SPT). This system entailed labeling surface CX_3CL1 at an intermediate density with primary antibody, followed by biotinylated secondary Fab fragments, and, finally, streptavidin-coated quantum dots. Caution was taken to limit the formation of CX_3CL1 clusters by blocking excess binding sites on the quantum dots with soluble biotin (see *Materials and Methods*). Using this approach, we were able to limit photobleaching, record videos at a frame rate of 30 Hz for 300 frames, and reconstruct CX_3CL1 trajectories using a multiparticle tracking algorithm (Jaqaman *et al.*, 2011). This algorithm uses moment scaling spectrum (MSS) analysis, identifying both mode of diffusion and diffusion coefficient.

Whereas primary ECs express minimal levels of CX_3CL1 under noninflammatory conditions, robust levels of the chemokine appear on the cell surface after exposure to tumor necrosis factor α (TNF-α; unpublished data). Using TNF-α–stimulated ECs, we tracked the mobility of endogenous, cell surface CX_3CL1 and found that $81.0 \pm 1.5\%$ experienced confined motion, whereas $18.0 \pm 1.0\%$ experienced free motion (Figure 1, A–D, and Supplemental Movie S1). These results were surprising, as this level of confinement is much greater than what has been described for other membrane-spanning proteins (Treanor *et al.*, 2010; Jaqaman *et al.*, 2011; Jaumouille *et al.*, 2014). Furthermore, we found that the confined population moved with a diffusion coefficient of 0.028 ± 0.005 μm^2/s and was restricted to a mean confinement area of 0.036 ± 0.003 μm^2 (Figure 1, D and E). CX_3CL1, however, experienced a broad range of confinement areas, indicating a heterogeneous population (Figure 1, E and F). To confirm that we were visualizing only surface CX_3CL1 and that labeling with antibody did not cause internalization of the chemokine, we exposed cells to an acid wash to dissociate extracellular antibody while preserving cell integrity. Less than 10% of the labeled CX_3CL1 remained after the acid wash, indicating that surface rather than internalized CX_3CL1 was being detected (unpublished data).

It is conceivable that the quantum dot probes used may cause artefactual confinement of CX_3CL1 molecules. To address this concern, we performed SPT of the chemokine using secondary Fab

fragments conjugated to the small fluorophore Cy3. Although the signal-to-noise ratio of Cy3 is much less than that of a quantum dot, we found similar fractions of CX_3CL1 undergoing confined and free motion (77.0 ± 1.4 and $21.0 \pm 1.2\%$, respectively) and measured comparable diffusion coefficients (Supplemental Figure S1, A and B). These findings demonstrate that the detected confinement of CX_3CL1 is not due to artificial clustering or cross-linking but is in fact an inherent property of the chemokine itself.

Although confined, CX_3CL1 molecules were clearly mobile (diffusion coefficient of 0.028 μm^2/s), suggesting that they are not anchored to a fixed structure but instead diffusing within a membrane corral. To validate the restricted mobility of CX_3CL1, we performed SPT using fixed samples. We reasoned that if the detection limit of our experimental system had not been reached, fixation would further reduce the mobility of CX_3CL1. Accordingly, fixation increased confined motion from 81.0 ± 1.5 to $95.0 \pm 0.5\%$ ($p <0.0001$), decreased free motion from 18.0 ± 1.0 to $4.6 \pm 0.6\%$ (Supplemental Figure S1D; $p < 0.0001$), and, of importance, decreased the diffusion coefficient of the confined molecules from 0.028 ± 0.005 to 0.005 ± 0.001 μm^2/s (Supplemental Figure S1E; $p < 0.0001$). Fixation also resulted in a decrease in confinement area from 0.036 ± 0.003 to 0.007 ± 0.002 μm^2 (Figure 1, E and F, $p < 0.0001$). Taken together, these results suggest that in live cells, CX_3CL1 is not completely immobile but instead moves within confined regions of the plasma membrane.

CX_3CL1 is not confined by caveolae or membrane rafts

The preceding results led us to question how CX_3CL1 might be confined within regions of the plasma membrane. We reasoned that CX_3CL1 could be associated with cholesterol-enriched membrane domains, such as rafts or caveolae, which have been shown to restrict membrane protein diffusion (Thomsen *et al.*, 2002; Pelkmans *et al.*, 2004; Sinha *et al.*, 2011). Caveolae are particularly abundant in ECs, and thus we assessed the colocalization of CX_3CL1 and the caveolar protein, caveolin-1, using single-molecule subdiffraction imaging (Figure 2A; see *Materials and Methods* for details). This approach, termed spatial apposition analysis (SAA), involved labeling both proteins with subsaturating concentrations of primary antibody, followed by fluorescent secondary Fab fragments, and has been validated (Heit *et al.*, 2013). The relative distances between CX_3CL1 and caveolin-1 particles were measured next using a nearest-neighbor approach and compared with a randomly generated distribution of the same particles (Figure 2A). We then compared the fraction of particle pairs within a predetermined colocalization distance criterion (CDC) in both measured and random populations. As shown in Figure 2B, the amount of colocalization between CX_3CL1 and caveolin-1 did not differ significantly from a predicted random distribution, indicating that the two proteins are not associated on the surface of endothelial cells. We verified the ability of the SAA to detect colocalization by using a Fab$_2$ to cross-link CX_3CL1 and TACE, two proteins with limited interactions under basal conditions (Tole *et al.*, 2010). As reflected in our analysis, the amount of colocalization between these proteins initially did not differ significantly from that of a predicted random distribution (Supplemental Figure S2, A and B). However, upon cross-linking, we detected significant colocalization between CX_3CL1 and TACE, thereby supporting the use of our system to detect protein interactions (Supplemental Figure S2, C and D).

To confirm that CX_3CL1 is not confined by caveolae, we treated ECs with methyl-β-cyclodextrin (MβCD) to deplete cholesterol, thus disassembling caveolae, and assessed the distribution of the chemokine. As expected, treatment with MβCD depleted 60% of
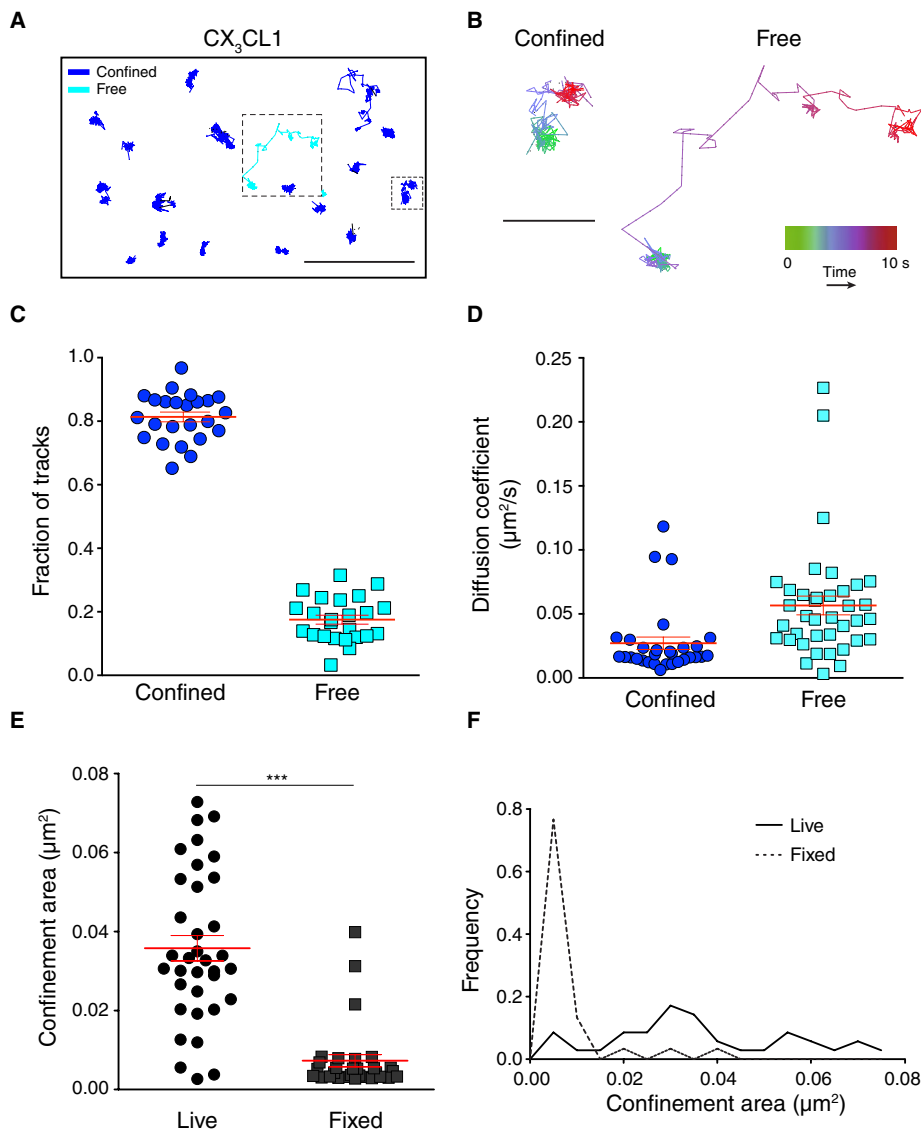
A

CX₃CL1

- ■ Confined
- ■ Free

B

Confined   Free

0   Time   10 s

C

D

E

F

FIGURE 1: CX₃CL1 is confined, but not immobile on the surface of ECs. (A) ECs were incubated with TNF-α for 4 h, and cell-surface CX₃CL1 was detected by quantum dot labeling (see *Materials and Methods*). SPT was performed using videos recorded at 30 Hz for 300 frames. Motion was determined using MSS analysis and custom algorithms in Matlab. Representative tracks of surface CX₃CL1. Dotted black lines represent tracks with unclassified motion, and solid black lines represent the closing of gaps. Scale bar, 1 µm. (B) Magnified confined and free trajectories from A (insets) color coded based on time (green to blue to red, ~10 s). Scale bar, 0.5 µm. (C) Fraction of CX₃CL1 particles experiencing confined or free motion in the plasma membrane. (D) Diffusion coefficients of confined and free CX₃CL1 were determined by MSS analysis. (E) CX₃CL1 confinement area values and (F) distribution of confinement area in live and fixed cells. Individual data points represent the median value of particles from a single field of view. Data are mean ± SEM of the medians from five independent experiments with >5 fields of view analyzed per experiment. Typical fields of view were ~34 × 34 µm in size with 50–200 particles. ***$p < 0.0001$.

After depletion of cholesterol, however, we were unable to detect a significant change in either mode of diffusion or confinement area (Figure 2, D and E). In fact, treatment with MβCD actually decreased both CX₃CL1 confined and free diffusion coefficients (Figure 2F), similar to what has been reported for other membrane proteins (Fujiwara *et al.*, 2002; Murase *et al.*, 2004). Taken together, these results demonstrate that CX₃CL1 is not confined by caveolae or cholesterol-enriched membrane microdomains.

CX₃CL1 is confined by the actin cytoskeleton

Emerging evidence indicates that the cortical actin meshwork plays a role in regulating the mobility and distribution of membrane-associated proteins (Goswami *et al.*, 2008; Chung *et al.*, 2010; Treanor *et al.*, 2010; Jaqaman *et al.*, 2011; Gowrishankar *et al.*, 2012). To determine whether the organization of actin affects the confinement of CX₃CL1, we treated cells with calyculin A (Cal A), which stimulates myosin II activity by inhibiting the myosin phosphatase. By stimulating myosin-mediated contractility, Cal A treatment induced the compaction of the actin cytoskeleton to the center of the cell, generating membrane blebs devoid of cortical actin (Figure 3A; Henson *et al.*, 2003). Incubation of cells with blebbistatin, an inhibitor of myosin IIa, greatly reduced the formation of membrane blebs, confirming that Cal A compaction of the cytoskeleton is indeed myosin dependent (Supplemental Figure S3A). We hypothesized that if CX₃CL1 was associated with actin through direct or indirect interactions, incubation with Cal A would cause the chemokine to accumulate near the center of the cell, along with the contracted cytoskeleton. Accordingly, we found that Cal A caused CX₃CL1 to concentrate near the center of cells, colocalizing with the actin cytoskeleton (Figure 3B and Supplemental Figure S3B). To verify that this was not a general effect of Cal A on all membrane proteins, we examined its effects on the localization of a protein associated with the plasma membrane outer leaflet, glycosyl-phosphatidylinositol–linked green fluorescent protein (GPI-GFP), as well as a protein associated electrostatically with the inner leaflet, the tail of K-Ras (K-Ras-GFP; Yeung *et al.*, 2006). In contrast to CX₃CL1, Cal A treatment caused both GPI-GFP and K-Ras-GFP to enter membrane blebs devoid of cortical actin (Figure 3, A and C). Of importance, GT-46 (GT-46–yellow fluorescent protein [YFP]), a chimeric transmembrane protein that is not associated with lipid rafts (Kenworthy *et al.*, 2004), also localized to membrane blebs (Figure 3D). These results demonstrate that association with the cytoskeleton is a unique feature of CX₃CL1 rather than a property shared by all membrane proteins.

cell cholesterol (Supplemental Figure S2, E and F) and disassembled caveolae, causing caveolin-1 to become uniformly distributed (Figure 2C). CX₃CL1 distribution, however, remained unchanged, further supporting the notion that it is not associated with caveolae (Figure 2C).

The possibility of rafts and caveolae confining CX₃CL1 was finally discounted by performing SPT after treatment with MβCD. We hypothesized that if these membrane domains confined CX₃CL1, depleting cholesterol would yield a measurable increase in mobility.
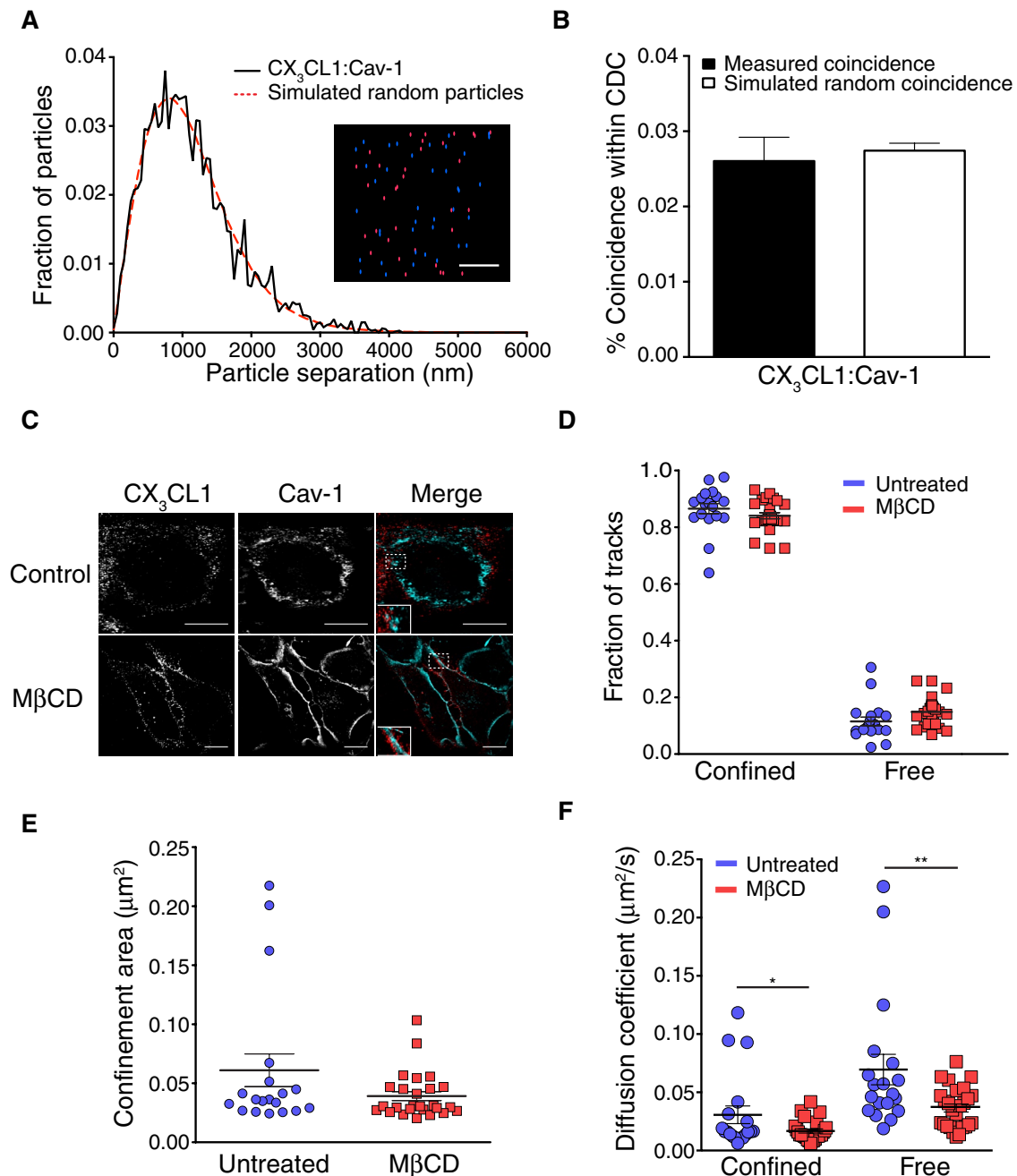
FIGURE 2: CX₃CL1 is not confined by caveolae or cholesterol-rich membrane domains. (A) Single-molecule SAA of cell surface CX₃CL1 and Cav-1. ECs were incubated with TNF-α and labeled with primary antibody, followed by fluorescent Fab fragments, detecting CX₃CL1 and caveolin-1 at low densities. Experimentally measured particle distribution (solid black line) was compared with a predicted random distribution (dashed red line). Representative histogram depicting the spatial association between CX₃CL1 and Cav-1 at the subdiffraction level. Reconstructed image of CX₃CL1 (blue) and Cav-1 (red) after subdiffraction localization. Scale bar, 3 μm. (B) Comparison of the spatial association between CX₃CL1 and caveolin-1 particles. The fraction of particle pairs within a predetermined colocalization cutoff was compared between the experimentally measured population (measured coincidence) and the predicted, random population (simulated random coincidence). The CDC was determined as described in *Materials and Methods*. For A and B, analysis was based on 3192 particle pairs from four independent experiments, combining >10 fields per experiment. (C) Spinning-disk confocal fluorescence images of cell surface CX₃CL1 and caveolin-1 before and after depleting cholesterol with MβCD. Images are representative of three independent experiments. Insets, magnified view of indicated area. Scale bar, 15 μm. (D) Fraction of CX₃CL1 particles experiencing confined and free motion. (E) Diffusion coefficients of confined and free CX₃CL1 after MβCD treatment. (F) CX₃CL1 confinement area after treatment with MβCD determined by SPT. Individual data points represent the median value of particles from a single field of view. Data are mean ± SEM of the medians from four independent experiments with 5–10 fields of view analyzed per experiment. *$p < 0.05$, **$p < 0.001$.
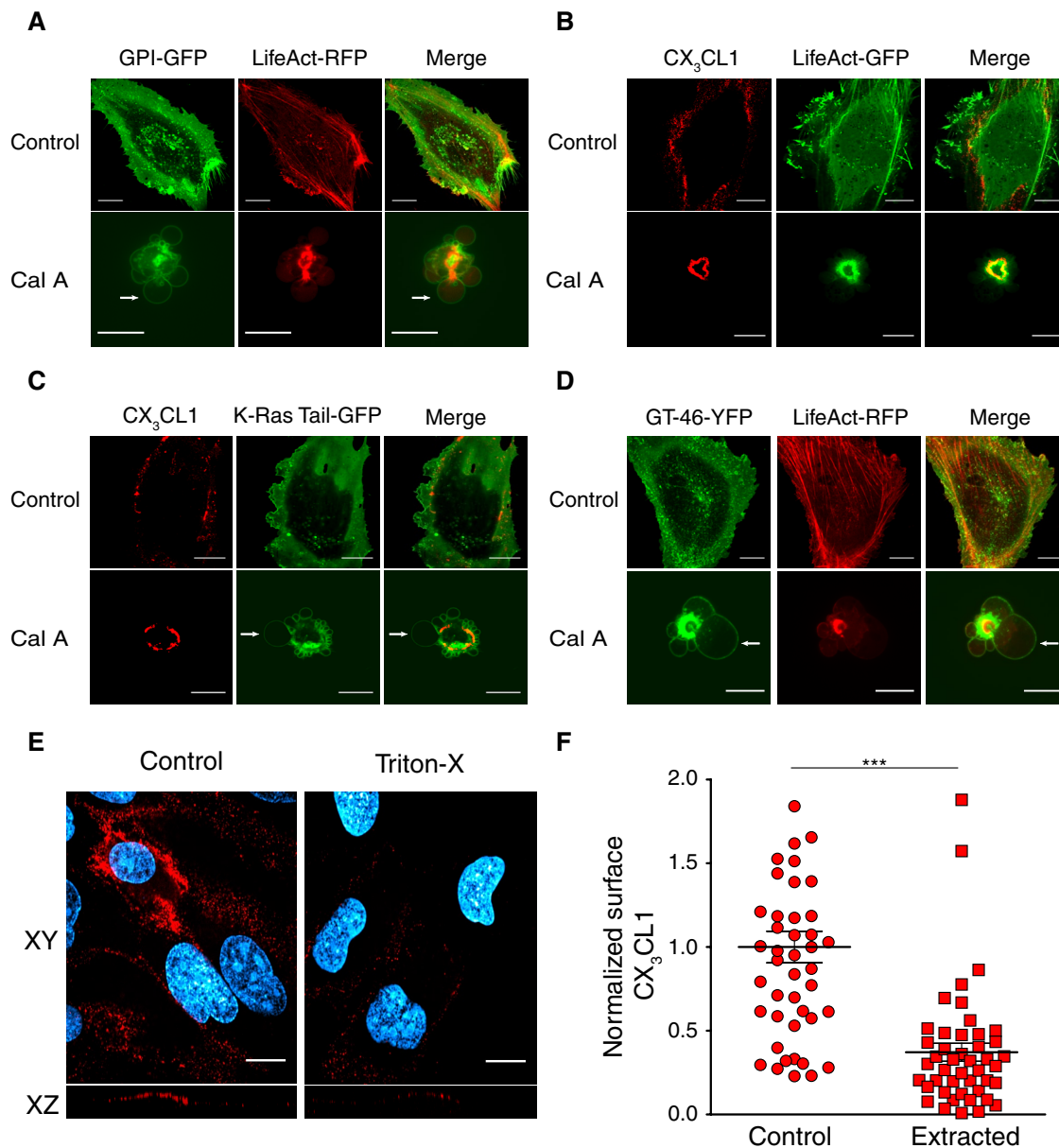
FIGURE 3: CX$_3$CL1 is associated with the actin cytoskeleton. (A) Representative spinning-disk confocal fluorescence images of live ECs transfected with expression plasmids encoding the outer leaflet protein, GPI-GFP, as well as LifeAct-RFP to visualize F-actin. (B) ECs were transfected with plasmids encoding CX$_3$CL1-mCherry and LifeAct-GFP. Cells were incubated with Cal A, and cell surface CX$_3$CL1 was visualized by incubating cells at 10°C with anti-CX$_3$CL1 Ab followed by Alexa 647–conjugated anti-goat IgG. Representative spinning-disk confocal fluorescence images. (C) ECs were transfected with plasmids encoding CX$_3$CL1 and an inner leaflet protein, K-Ras Tail-GFP. Experiments were performed as in B. Representative spinning-disk confocal fluorescent images. (D) ECs were transfected with plasmids encoding GT-46-YFP and LifeAct-RFP. Experiments were performed as in B. Representative spinning-disk confocal fluorescent images. For A–D, images are representative of three independent experiments. Arrows indicate membrane blebs devoid of actin. Scale bars, 15 µm. (E) ECs were incubated with anti-CX$_3$CL1 Ab, followed by DyLight 549–conjugated anti-goat Fab fragment, treated with Triton-X, and fixed. Cells were then incubated with Draq 5 (blue) to visualize nuclei. Representative *XY* and *XZ* optical slices obtained using spinning-disk confocal microscopy. (F) Quantification of cell surface CX$_3$CL1 from E (see *Materials and Methods*). Data are mean ± SEM of three independent experiments, each containing 15 fields of view and at least 50 cells. ***$p < 0.0001$.

When combined with the SPT analyses, these findings suggest that CX$_3$CL1 is fenced within actin-delimited "corrals" yet not firmly bound to them. To test this notion, we performed membrane extractions using nonionic detergents in a cytoskeleton-stabilizing buffer (see *Materials and Methods* for details). As shown in Figure 3, E and F, a large fraction (63%) of CX$_3$CL1 was lost from the membrane upon extraction ($p < 0.0001$ vs. control). This confirms that CX$_3$CL1 is not stably associated with the cytoskeleton and suggests that the observed mobility of the chemokine is a reflection of its free diffusion within corrals rather than motion restricted by a flexible,
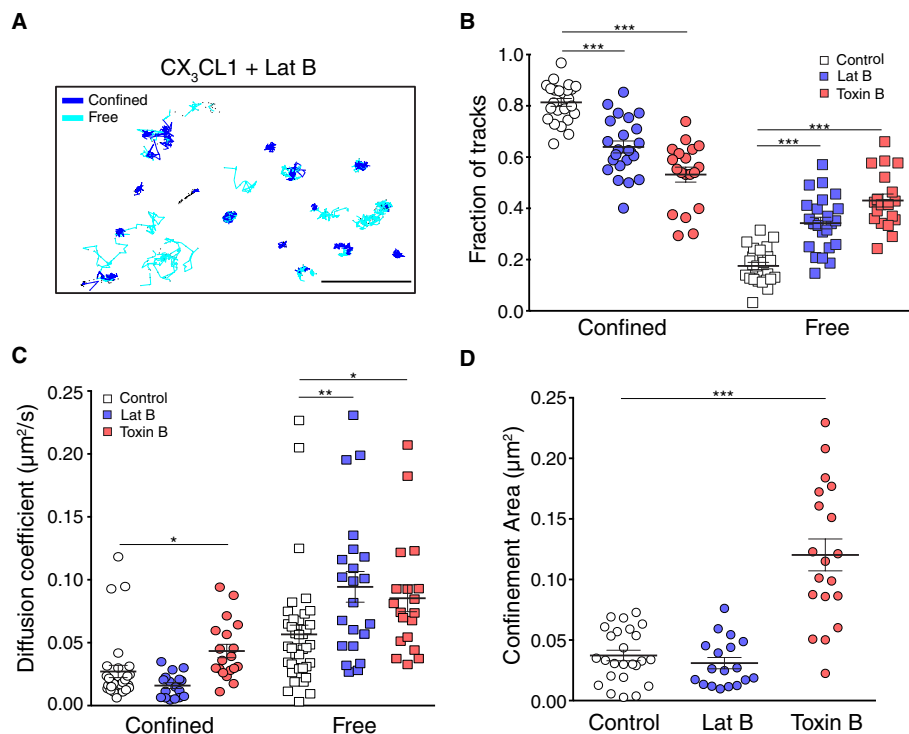
FIGURE 4: CX₃CL1 confinement in the plasma membrane depends on the actin cytoskeleton. (A) Cells were incubated with either Lat B or Toxin B, and SPT of cell surface CX₃CL1 was performed as in Figure 1. Representative tracks of surface CX₃CL1 in Lat B–treated cells. Scale bar, 3 μm. (B) Fraction of CX₃CL1 particles experiencing confined and free motion after treatment with Lat B or Toxin B. (C) Confined and free diffusion coefficients for CX₃CL1 after disruption of actin using Lat B or Toxin B. (D) CX₃CL1 confinement area following treatment with Lat B or Toxin B. Individual data points represent the median value of particles from a single field of view. Data are mean ± SEM of the medians from at least three independent experiments with 5–15 fields of view analyzed per experiment. *$p < 0.05$, **$p < 0.001$, ***$p < 0.0001$.

stable tether. However, the possibility that the gentle nonionic detergent used dislodged CX₃CL1 from a cytoskeletal attachment site cannot be discounted.

CX₃CL1 mobility is restricted by the actin cytoskeleton

If CX₃CL1 is indeed trapped within cytoskeletal corrals, disruption of actin filaments should decrease the chemokine's confinement. To this end, we treated ECs with either latrunculin B (Lat B), which sequesters actin monomers, or *Clostridium difficile* toxin B (Toxin B), which inhibits Rho-family GTPases, particularly Rac and Cdc42 (Supplemental Figure S3C; Just *et al.*, 1994). Minimum concentrations and incubation times were used to prevent the detachment of cells from the coverslip. After incubation with either Lat B or Toxin B, we performed SPT of CX₃CL1 and found a considerable decrease in confined motion and an accompanying increase in free motion (Figure 4, A and B, and Supplemental Movie S2; $p < 0.0001$ vs. control). Lat B also greatly increased the free diffusion coefficient to 0.094 ± 0.012 μm²/s (Figure 4C; $p < 0.01$ vs. control), whereas Toxin B increased both the confined and free diffusion coefficients to 0.043 ± 0.005 s and 0.085 ± 0.010 μm²/s (Figure 4C; $p < 0.05$ vs. control), respectively, as well as the confinement area to 0.120 μm² (Figure 4D, $p < 0.0001$ vs. control). The more pronounced effect of Toxin B on CX₃CL1 confinement likely reflects the fact that it disrupted the cortical cytoskeleton to a greater extent than Lat B (unpublished data). Of note, higher concentrations of Lat B resulted in gross morphological changes, causing many ECs to collapse or detach from the coverslip. Toxin B, on the other hand, induced global reorganization of the cytoskeleton yet maintained cell structure (Supplemental Figure S3C). These results indicate that the confinement regions, to which CX₃CL1 diffusion is restricted, depend on the integrity of actin.

The cytoplasmic domain of CX₃CL1 influences confinement by the cytoskeleton

The intracellular domains of immune receptors, such as the B-cell receptor (BCR), have been shown to influence their diffusion dynamics (Treanor *et al.*, 2010). Thus we asked whether the intracellular domain of CX₃CL1 contributed to its confinement by the cytoskeleton. To investigate this possibility, we expressed a truncated allele of CX₃CL1, lacking the intracellular domain of the chemokine (CX₃CL1-360), and tracked its mobility using SPT (Figure 5, A and B, and Supplemental Movie S3; Huang *et al.*, 2009). To account for changes in mobility that could result from overexpression, we transfected ECs with a full-length CX₃CL1 plasmid in parallel. Of importance, ECs were not treated with TNF-α, to avoid confounding effects of the endogenous chemokine. Under these conditions, full-length CX₃CL1 demonstrated similar diffusion characteristics compared with endogenous CX₃CL1 in TNF-α–treated EC (Figures 1, A–E, and 5, C and D). In sharp contrast, CX₃CL1-360 experienced a marked decrease in confined motion, from 78.0 ± 3.0 to 33.0 ± 2.0%, and an increase in free motion, from 20.0 ± 3.0 to 60.0 ± 2.0% (Figure 5C, $p < 0.0001$ vs. full-length CX₃CL1). CX₃CL1-360 also displayed a significant increase in its confined diffusion coefficient, from 0.025 ± 0.002 to 0.050 ± 0.005 μm²/s (Figure 5D; $p < 0.0001$ vs. full-length CX₃CL1), as well as in its confinement area, from 0.050 to 0.166 μm² (Figure 5, E and F; $p = 0.0001$ vs. full-length CX₃CL1), suggesting that it could more readily hop between actin corrals. These results demonstrate that the intracellular domain of CX₃CL1 plays a critical role in its confinement by the actin cytoskeleton.

CX₃CL1 is segregated from ADAM10 within the plasma membrane

The confined distribution of CX₃CL1 in the plasma membrane might explain why the chemokine is not readily accessible and fully cleaved by the plasmalemmal, transmembrane metalloprotease ADAM10, which is constitutively active (Hundhausen *et al.*, 2003). To investigate this possibility, we performed SPT of ADAM10 using a similar labeling procedure to that of CX₃CL1 and found that 56.0 ± 2.0% of the protease experienced confined motion, moving with a diffusion coefficient of 0.012 ± 0.001 μm²/s, whereas 41.0 ± 2.0% experienced free motion, with a diffusion coefficient of 0.051 ± 0.003 μm²/s (Supplemental Movie S4 and Figure 6, A–D). Furthermore, the confined population of ADAM10 was restricted to a mean area of 0.034 ± 0.002 μm² (Figure 6, E and F). These results greatly differ from the SPT measurements of CX₃CL1, indicating that the mobility of these two transmembrane proteins is dictated by different determinants (Figure 1, A–F).
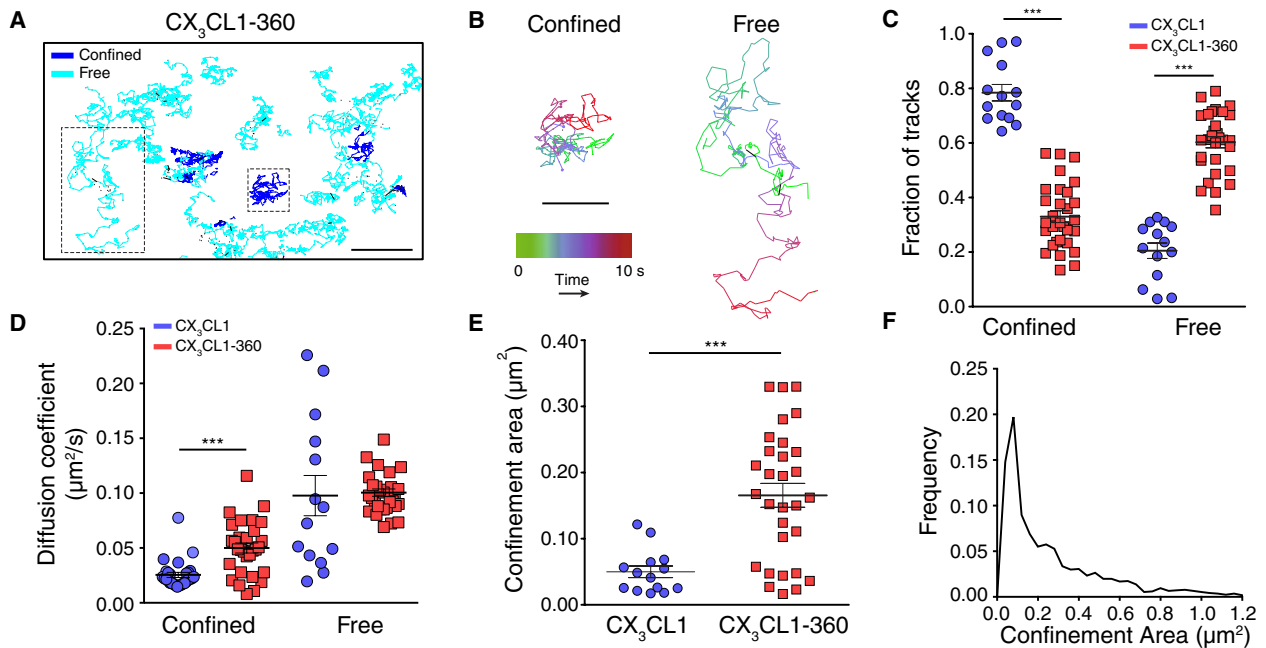
FIGURE 5: The intracellular domain of CX_3CL1 determines confinement. (A) ECs were transfected with an expression plasmid encoding CX_3CL1-360, which lacks the intracellular domain of the chemokine, and SPT performed as in Figure 1. Representative tracks of the truncated CX_3CL1-360. Scale bar, 3 µm. (B) Magnified confined and free trajectories from A (insets) color coded based on time (green to blue to red, ~10 s). Scale bar, 1.5 µm. (C) ECs were transfected with plasmids encoding full-length CX_3CL1 or truncated CX_3CL1-360 and SPT performed as in A. Fraction of CX_3CL1 and CX_3CL1-360 particles experiencing confined and free motion. (D) Confined and free diffusion coefficients calculated for full-length CX_3CL1 and truncated CX_3CL1-360. (E) Confinement areas of full-length CX_3CL1 and truncated CX_3CL1-360 particles. (F) Distribution of confinement area for CX_3CL1-360. Individual data points represent the median value of particles from a single field of view. Data are mean ± SEM of the medians from three independent experiments with 10 fields of view analyzed per experiment. ***$p \leq 0.0001$.

Our data imply that there are distinct confined and free subpopulations of ADAM10. We initially questioned whether CX_3CL1 and ADAM10 coexist in the same confinement regions, possibly accounting for the modest, yet significant basal cleavage of CX_3CL1. To test this possibility, we used single-molecule imaging and the SAA to assess the localization of both proteins at the subdiffraction level. Surprisingly, we found that the percentage of CX_3CL1 and ADAM10 particle pairs within the predetermined CDC was in fact significantly less than that predicted for a random distribution (Figure 6, G and H; $p < 0.0001$ measured vs. random). Thus a mechanism of active segregation exists between the two transmembrane proteins. These results demonstrate that within the plasma membrane, CX_3CL1 and ADAM10 are not significantly associated or co-confined. Instead, it appears that at small distances, ADAM10 is physically restricted from interacting with CX_3CL1.

The actin cytoskeleton controls shedding of cell surface CX_3CL1

Given that ADAM10 is constitutively active and a large fraction is mobile, we asked what factors limited its accessibility to the majority of CX_3CL1, preventing complete shedding of the latter from the cell surface. We hypothesized that the CX_3CL1 confinement regions, which depend on the integrity of actin, may limit access of ADAM10 to the chemokine. To test this notion, we disrupted the actin cytoskeleton with Lat B and again used single-molecule SAA to assess the localization of both proteins. Cells were initially pretreated with the ADAM10 inhibitor G1254023X to prevent excess shedding of CX_3CL1 that could result from disrupting the cytoskeleton, since this would severely limit the chance of detecting of colocalization. In the

presence of G1254023X, active segregation between CX_3CL1 and ADAM10 was recapitulated. Remarkably, after treatment with Lat B, we detected significant colocalization between CX_3CL1 and ADAM10 compared with that predicted for a random distribution (Figure 7, A and B; $p < 0.05$ measured vs. random). These results demonstrate that the cortical actin cytoskeleton physically limits interactions between CX_3CL1 and ADAM10.

Functionally, increased CX_3CL1 and ADAM10 interactions should decrease the amount of transmembrane chemokine present on the cell surface and increase the amount of soluble chemokine released. To this end, we again took advantage of Toxin B to disrupt the cortical actin and examined the effects on the proteolytic cleavage of CX_3CL1 (Figure 7, C and D). Strikingly, exposure to Toxin B reduced levels of CX_3CL1 present at the cell surface by 40% (Figure 7D; $p < 0.05$ vs. control). A similar 47% decrease was obtained using Lat B (Supplemental Figure S4, A and B, $p < 0.05$ vs. control). To determine whether the decrease in cell surface CX_3CL1 was in fact due to proteolytic shedding of the chemokine, we incubated cells with the metalloprotease inhibitor TAPI-2, which inhibits ADAM10 (Tole et al., 2010). Exposure to TAPI-2 prevented the observed decreases in cell surface CX_3CL1 induced by both Toxin B and Lat B (Figure 7, C and D, and Supplemental Figure S4, A and B; $p < 0.0001$ vs. Toxin B or Lat B alone). Most important, treatment with Toxin B also increased the release of soluble CX_3CL1 (Figure 7E; $p < 0.05$ vs. untreated), an effect prevented by metalloprotease inhibition (Figure 7E; $p < 0.0001$ vs. Toxin B alone).

We next sought to confirm that the increased cleavage of CX_3CL1 after disruption of the actin cytoskeleton was specifically due to ADAM10. Thus we performed gene silencing of ADAM10 using

small interfering RNA (siRNA), followed by treatment of the ECs with Toxin B (Figure 7F). Similar to effects seen with TAPI-2, knockdown of ADAM10 prevented the decrease in cell surface CX_3CL1 induced by Toxin B, an effect not seen in cells treated with scrambled siRNA as a control (Figure 7, F and G; $p < 0.0001$ scrambled siRNA vs. ADAM10 siRNA).

Previously, we reported that CX_3CL1 contained two putative adaptor protein-2 (AP-2)–binding domains and that inhibition of clathrin-mediated endocytosis enhanced ADAM-dependent shedding of the chemokine (Huang et al., 2009). Thus it is conceivable that disrupting the actin cytoskeleton may disrupt clathrin-mediated endocytosis of CX_3CL1 and increase proteolytic cleavage by ADAM10. This concern was addressed by assessing the internalization of transferrin, as well as of CX_3CL1, in the presence of Lat B. Disrupting the actin cytoskeleton had little effect on internalization of both proteins (Supplemental Figure S5, A–C). Furthermore, we performed SPT of a mutant CX_3CL1 (CX_3CL1-Y362A-Y392A) in which alanine residues were substituted for the tyrosine residues of both AP-2–binding motifs previously shown to be critical for endocytosis (Huang et al., 2009). Unlike what was observed with CX_3CL1-360, CX_3CL1- Y362A-Y392A displayed no significant changes in lateral mobility compared with control, full-length CX_3CL1 (Figure 5C and Supplemental Figure S5D). Therefore our results cannot be explained by disruption of clathrin-mediated endocytosis but instead support the notion that shedding of the chemokine is regulated by the actin cytoskeleton.

If actin confinement regions limit interactions between CX_3CL1 and ADAM10, then CX_3CL1-360, which is only $33.0 \pm 2.0\%$ confined, should be cleaved significantly more than full-length CX_3CL1 (Figure 5C). To test this hypothesis, we initially compared the amount of cell surface CX_3CL1 in EC expressing full-length or truncated CX_3CL1. As expected, after normalization for expression levels, significantly less chemokine (~ 60% less) was detected at the plasma membrane in cells expressing CX_3CL1-360 (Figure 7, H and I; $p < 0.0001$ vs. full-length CX_3CL1). However, these results do not account for potential differences in trafficking that truncated CX_3CL1-360 may experience. To control for this possibility, we performed an enzyme-linked immunosorbent assay (ELISA) to measure the release of soluble chemokine in ECs again expressing either full-length or truncated CX_3CL1. In parallel, cells were treated with G1254023X, which allowed us to calculate the fraction of CX_3CL1 cleaved by ADAM10 and normalize for possible changes in trafficking to the plasma membrane (see Materials and Methods). As Figure 7J illustrates, CX_3CL1-360 was shed approximately twofold more by ADAM10 than with full-length CX_3CL1 ($p < 0.0001$). This implies that less confinement does indeed result in more ADAM10-dependent proteolytic cleavage. Overall these results demonstrate that disrupting the actin cytoskeleton leads to ADAM10-mediated cleavage of cell surface CX_3CL1 and the concomitant release of the soluble form of the chemokine.

DISCUSSION

Our results indicate that 1) CX_3CL1 is confined in regions of the plasma membrane by the cortical actin meshwork, and 2) this confinement results in segregation of CX_3CL1 from ADAM10, limiting basal proteolytic cleavage and the release of soluble chemokine. Membrane proteins can be influenced by the cytoskeleton in two distinct ways. The first involves direct or indirect anchoring or tethering to the cytoskeleton (Haggie et al., 2006; Chen et al., 2009; Jaqaman and Grinstein, 2012). The second involves the creation of cytoskeletal barriers, which limit protein diffusion (Kusumi et al., 2005a). Our observation that confined CX_3CL1 displays measurable

diffusion and that a large fraction of CX_3CL1 is lost from the cell surface after membrane extraction does not support the first scenario. Instead, our data suggest that the cortical actin cytoskeleton compartmentalizes the membrane, restricting CX_3CL1 diffusion to corrals of varying size. Note, however, that the confinement of CX_3CL1 is observed throughout acquisition periods of ~10 s, differing from the short-term, hop diffusion events observed by Kusumi et al. (2005b) at the microsecond time scale. Because a fraction of CX_3CL1 remained associated with the insoluble fraction after membrane extraction, we cannot rule out that the plasmalemmal pool of the chemokine is heterogeneous, with a small subpopulation stably tethered to actin, whereas the majority diffuses isotropically within actin corrals.

Given the time scale used for SPT, we are unable to distinguish whether our observations represent total confinement of a small population of CX_3CL1 molecules or temporary confinement of the majority of CX_3CL1. However, our data do indicate that CX_3CL1 molecules are strongly trapped within the actin network. Indeed, the chemokine colocalizes with the compacted cytoskeleton upon treatment with Cal A, unable to escape the dense filamentous meshwork. This suggests that the majority of CX_3CL1 may experience transient interactions with actin or actin-associated molecules, leading to its recruitment to the cortical cytoskeleton by a diffusion and capture mechanism (Rudner et al., 2002). Although the exact mechanism of confinement remains to be determined, it is likely that trapping of CX_3CL1 within corrals occurs through interactions with another membrane protein complex directly linked to the cytoskeleton. The identity of this protein complex remains to be determined; however, CX_3CL1 has previously been suggested to interact with the endothelial adhesion molecule VCAM-1 to support leukocyte recruitment (Kerfoot et al., 2003). Furthermore, on leukocytes, the receptor for VCAM-1, VLA-4, has been shown to exist in a complex with the receptor for CX_3CL1, CX_3CR1, implying that the two adhesion molecules may be associated (Fujita et al., 2012). Of importance, VCAM-1 is reported to anchor to the actin cytoskeleton through ezrin-radixin-moesin (ERM) proteins (Heiska et al., 1998; Barreiro et al., 2002). Thus it is conceivable that CX_3CL1 indirectly interacts with the actin cytoskeleton through transient associations with VCAM-1 and ERM protein complexes.

The restricted diffusion of transmembrane CX_3CL1 correlates with limited release of its soluble species. This raises the possibility that confinement influences the ability of CX_3CL1 to interact with ADAM10, regulating its rate of proteolytic cleavage. Of interest, recent Monte Carlo simulations demonstrated that cytoskeleton-based confinement of plasma membrane proteins could, under certain conditions, restrict protein collisions (Jaumouille et al., 2014). Thus, in principle, protein confinement could reduce the rate of collisions between CX_3CL1 and ADAM10, altering the frequency of CX_3CL1 cleavage. The effect of confinement, however, depends on several factors, including the surface densities of the protease and substrate, their respective diffusion coefficients, the time that the proteins are confined, and, finally, the size of the confinement regions. Thus, whereas at low surface densities membrane confinement would reduce the number of collisions (Jaumouille et al., 2014), at higher densities collision frequency may remain unaltered or even increase (Kalay et al., 2012). It is also noteworthy that not every collision between the protease and its substrate will result in a productive proteolytic event. If multiple collisions are required, as is likely the case, the effects of confinement on proteolysis would be greatly magnified: reduced collision rates would require much longer times to yield proteolysis and vice versa. In our studies, disruption of the cytoskeleton reduced CX_3CL1 confinement, increased
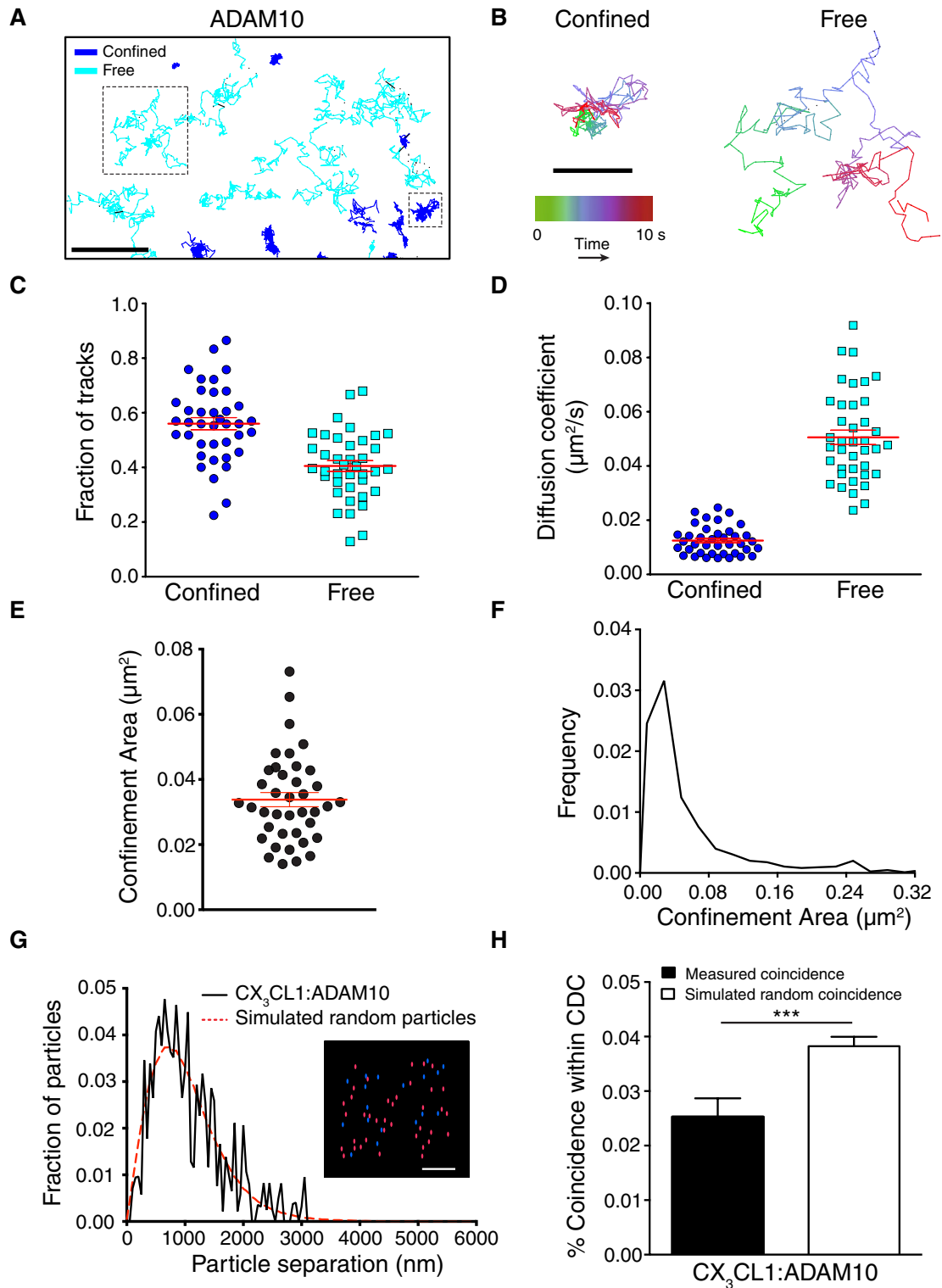
FIGURE 6: ADAM10 has limited interaction with CX₃CL1 on the surface of ECs. (A) ECs were incubated with TNF-α and surface ADAM10 detected by quantum dot labeling. SPT was performed as in Figure 1. Representative tracks of ADAM10. Scale bar, 1 µm. (B) Magnified confined and free trajectories from A (insets) color coded based on time (green to blue to red, ~10 s). Scale bar, 0.5 µm. (C) Fraction of ADAM10 particles experiencing confined and free motion. (D) Diffusion coefficient of ADAM10 was calculated as in Figure 1D. (E) ADAM10 confinement area values and (F) distribution of confinement area. For C–E, individual data points represent the median value of particles from a single field of view. Data are mean ± SEM of the medians from four independent experiments with 10 fields of view analyzed per experiment. (G) Single-molecule SAA of CX₃CL1 and ADAM10. ECs were treated with TNF-α and labeled with primary antibody, followed by fluorescent Fab fragments, detecting CX₃CL1 and ADAM10 at low densities. Experimentally measured particle distribution (solid black line) was compared with a predicted random distribution (dashed red line). Representative histogram depicting the spatial association between CX₃CL1 and ADAM10 at the

FIGURE 7: The actin cytoskeleton sequesters CX$_3$CL1 and limits its interactions with ADAM10. (A) Single-molecule SAA of CX$_3$CL1 and ADAM10. ECs were incubated with TNF-α, followed by treatment with the ADAM10 inhibitor G1254023X. Cells were incubated with Lat B, fixed, and labeled as in Figure 6. Experimentally measured particle distribution (solid black line) in Lat B–treated cells was compared with a predicted random distribution (dashed red line). Representative histogram depicting th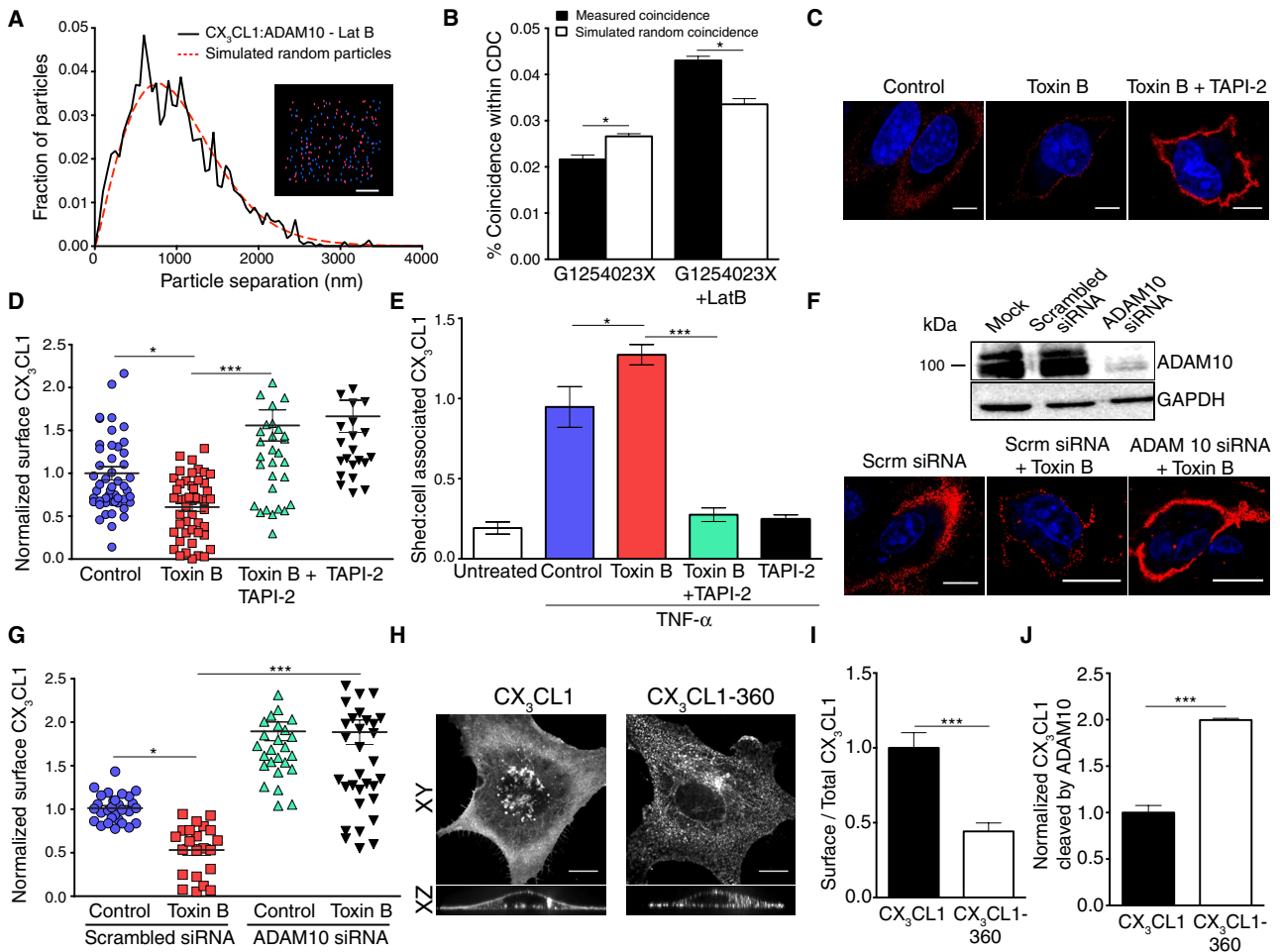e spatial association between CX$_3$CL1 and ADAM10 at the subdiffraction level. Reconstructed image of CX$_3$CL1 (blue) and ADAM10 (red) after subdiffraction localization. Scale bar, 3 μm. (B) The fraction of CX$_3$CL1 and ADAM10 particle pairs within a predetermined colocalization cutoff after treatment with Lat B was compared as in Figure 6H. For A and B, analysis was based on either 8539 particle pairs for G1254023X or 4435 particle pairs for G1254023X + Lat B from three independent experiments, combining 20 fields per experiment. Data are mean ± SEM. (C) ECs were incubated with TNF-α, exposed to Toxin B in the presence or absence of the metalloprotease inhibitor TAPI-2, fixed, and immunofluorescently labeled with Ab detecting CX$_3$CL1 (red) and with Draq5 nuclear stain (blue). Representative spinning-disk confocal images. Scale bars, 15 μm. (D) Cell surface CX$_3$CL1 was quantified as described in *Materials and Methods*. Data are mean values ± SEM of four independent experiments, each with 10 fields of view and at least 50 cells. (E) Experiments were performed as in C, and the amount of soluble CX$_3$CL1 was measured using an ELISA. Data represent the ratio between soluble CX$_3$CL1 detected in conditioned medium and CX$_3$CL1 detected in cell lysates. Data are mean values ± SEM from four independent experiments. (F) ECs were transfected with siRNA targeting ADAM10 or with scrambled nontargeting siRNA. Top, representative immunoblot performed using Ab detecting ADAM10. Bottom, cells were incubated with toxin B and cell surface CX$_3$CL1 detected as described in C. (G) Cell surface CX$_3$CL1 was measured as in C. Data are mean values ± SEM of three independent experiments each with 10–15 fields of view and at least 50 cells per experiment. (H) ECs were transfected with plasmids encoding full-length CX$_3$CL1 or truncated CX$_3$CL1-360. Representative *XY* and *XZ* optical slices were obtained using spinning-disk confocal microscopy. Scale bar, 15 μm. (I) Quantification of plasma membrane CX$_3$CL1 in H normalized for varying levels of expression between cells (see *Materials and Methods*). Data are mean values ± SEM of three independent experiments each with 10 cells quantified. ***$p < 0.0001$. (J) ECs were transfected as in H. Cells were incubated with DMSO vehicle control or with G1254023X, and the amount of soluble CX$_3$CL1 was measured using an ELISA. Cells were normalized for level of expression, and data are reported as the amount of ADAM10-dependent shedding (see *Materials and Methods*). *$p < 0.05$, ***$p < 0.0001$.

subdiffraction level. Reconstructed image of CX$_3$CL1 (blue) and ADAM10 (red) after subdiffraction localization. Scale bar, 3 μm. (H) The fraction of CX$_3$CL1 and ADAM10 particle pairs within a predetermined colocalization cutoff was compared between the experimentally measured population (measured coincidence) and the predicted, random population (simulated random coincidence). For G and H, analysis was based on 2291 particle pairs from three independent experiments, combining 20 fields per experiment. Data are mean ± SEM. ***$p < 0.0001$.
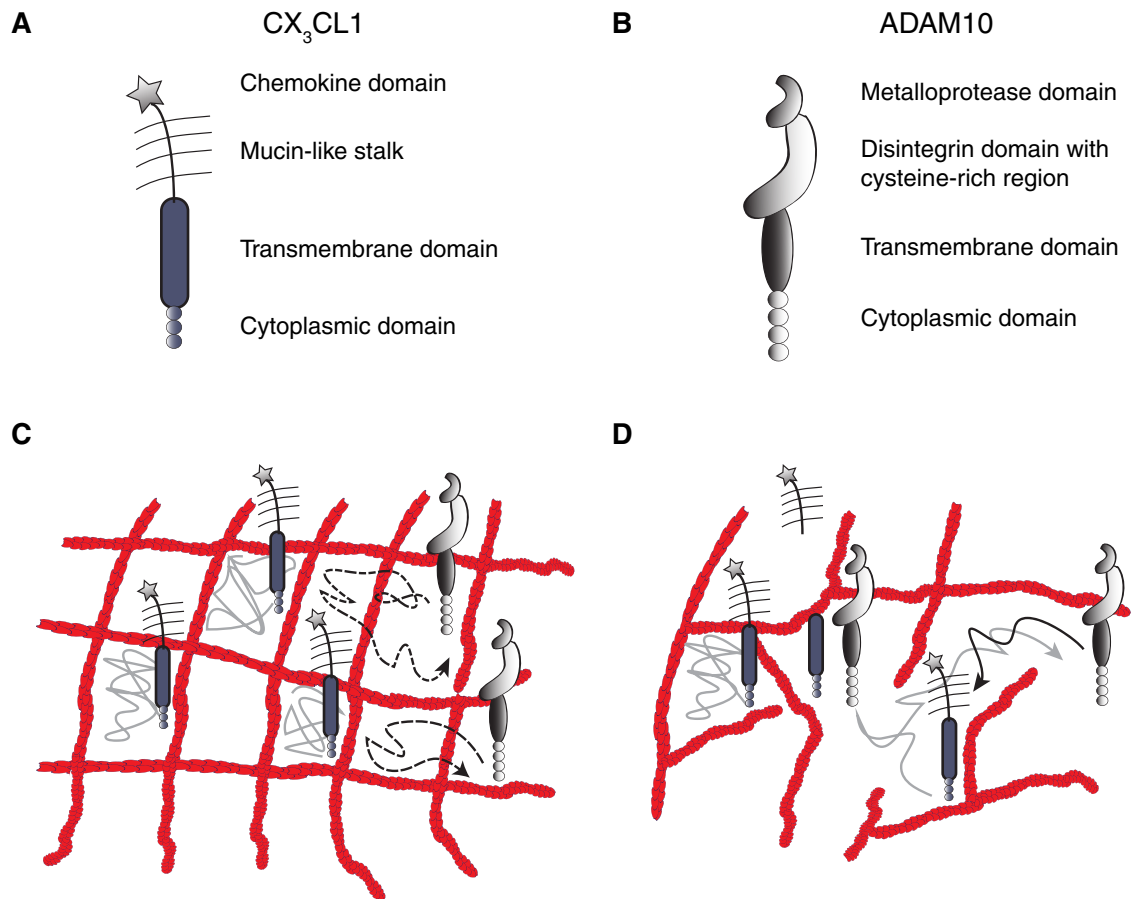
FIGURE 8: Model for cytoskeletal-regulated cleavage of plasma membrane CX$_3$CL1. (A) Schematic of the structure of CX$_3$CL1. (B) Schematic of the structure of ADAM10. (C) Proposed model for cytoskeletal-mediated exclusion between CX$_3$CL1 and ADAM10. CX$_3$CL1 diffusion is restricted due to actin confinement regions, which limit the access of ADAM10 to the chemokine. (D) Disruption of the cytoskeleton promotes convergence between CX3CL1 and ADAM10, and the subsequent release of soluble chemokine.

the diffusion coefficient of CX$_3$CL1, and promoted interactions with ADAM10, facilitating the proteolytic release of soluble chemokine. To this extent, our data seem most consistent with a model in which confinement reduces the likelihood of ADAM10 and CX$_3$CL1 converging and colliding.

Given the fact that ADAM10 plays a critical role in regulating the availability of adhesion molecules and ligands to various receptors expressed by circulating leukocytes, it is not surprising that such a spatial and temporal regulatory mechanism exists (Dreymueller *et al.*, 2012). The cytoskeleton was previously shown to restrict diffusion of membrane proteins, such as the BCR, Fcγ receptor, and CD36, thereby modulating their signaling. To our knowledge, this is the first demonstration that the actin cytoskeleton regulates physical contact between a membrane protease and its substrate (Treanor *et al.*, 2010; Jaqaman *et al.*, 2011; Jaumouille *et al.*, 2014). Several factors could regulate such an exclusion mechanism. Because ADAM10 has both a large confined and freely diffusing population, we envision three potential, yet not exclusive models for regulating cleavage of membrane substrates. In the first scenario, physiological stimuli may release or mobilize a confined substrate through reorganization of the cytoskeleton, greatly enhancing the accessibility of mobile ADAM10. Second, the release of a confined substrate may promote its interactions with confined ADAM10. Finally, the confined population of ADAM10 may be mobilized in response to

various stimuli, increasing its likelihood of encountering target substrate (Figure 8). Of interest, similar regulatory mechanisms involving differential compartmentalization of functionally associated membrane proteins have been described in other cell systems. For example, our results parallel what has been described for the BCR, which is confined by the actin cytoskeleton, and its coreceptor CD19. In this case, after disruption of the cytoskeleton, mobility of the BCR increases, favoring interactions with CD19, resulting in tonic or antigen-induced signaling (Treanor *et al.*, 2010; Mattila *et al.*, 2013). Therefore it would seem that membrane compartmentalization represents a general, biological phenomenon critical for regulating a wide variety of cellular functions. It is tempting to speculate that other ADAM10 substrates may be similarly protected from cleavage by the actin cytoskeleton.

It has been unclear how ADAM10 is regulated and whether its catalytic activity can be altered. Of interest, many of the pharmacologic agents that have been described to increase ADAM10 activity also drastically alter actin cytoskeleton dynamics. These agents include the calcium ionophore ionomycin, the RhoA activator thrombin, and the calmodulin inhibitor W7 (Hundhausen *et al.*, 2007; Schulz *et al.*, 2008; Prasain and Stevens, 2009; Beckers *et al.*, 2010). Thus the results obtained using these agents may reflect mobilization of confined substrates, such as CX$_3$CL1, or the mobilization of confined ADAM10. Both scenarios are consistent with our proposed

model of membrane compartmentalization. However, we cannot discount the possibility that disrupting actin filaments may inhibit an actin-sensitive protein that regulates ADAM10 activity or shields CX_3CL1 from cleavage. Note that although we found that cholesterol depletion did not affect the confinement of CX_3CL1, it has been reported to increase ADAM10-mediated shedding of the chemokine, as well as of other substrates (Matthews *et al.*, 2003; Murai *et al.*, 2011; Dreymueller *et al.*, 2012). It is possible that these results reflect mobilization of confined ADAM10 rather than a change in its catalytic activity.

What physiological stimuli could modulate cytoskeletal confinement regions? It is highly conceivable that in states of vascular inflammation, such as atherosclerosis, signals that cause reorganization of the endothelial cytoskeleton may affect CX_3CL1–ADAM10 interactions and thus influence the progression of disease. These signals could include secreted inflammatory molecules, physical interactions between leukocytes and ECs, or perhaps changes in mechanical force exerted on the endothelium. Indeed, atherosclerotic lesions develop in areas where fluid shear flow shifts from a laminar to a disturbed pattern (Cunningham and Gotlieb, 2005; Chiu and Chien, 2011). This transition in shear flow causes changes in both cytoskeletal orientation and cytoskeletal tension of vascular ECs (Chiu and Chien, 2011; Ting *et al.*, 2012). The random cytoskeletal orientation and decreased tension produced by disturbed shear flow may disrupt actin corrals within the EC membrane and increase the proteolytic release of soluble CX_3CL1. This in turn would promote recruitment of CX_3CR1-positive monocytes to the injured vascular wall, a cardinal feature of atherogenesis (Combadiere *et al.*, 2003; Lesnik *et al.*, 2003). Further work is required to test this hypothesis.

In summary, we reported here that the cortical actin cytoskeleton plays a critical role in regulating the diffusion of CX_3CL1 in the plasma membrane and in protecting the chemokine from proteolytic cleavage. We demonstrated a new mode of regulating proteolysis, in which the actin cytoskeleton acts as a barrier limiting physical contact between integral membrane proteases and their substrates. This novel cytoskeletal mechanism for controlling the availability of ligand on the surface of ECs could potentially be generalized to other metalloprotease substrates and may greatly contribute to the release of soluble inflammatory molecules. How such a regulatory mechanism is modulated by physiological or pathological stimuli in vivo remains a highly novel and exciting area of biology warranting further investigation.

MATERIALS AND METHODS

Cell culture and transfections
Primary human umbilical vein endothelial cells (HUVECs) were cultured in endothelial cell basal medium-2 (EBM-2; Clonetics, La Jolla, CA). For all experiments, only cells cultured for fewer than six passages were used.

Transient transfection of HUVECs was performed using Amaxa (Gaithersburg, MD) nucleofection or the NEON transfection system (Life Technologies, Burlington, Canada) as per the manufacturer's instructions. The expression plasmids used in this study include CX_3CL1-mCherry, CX_3CL1-360, CX_3CL1-Y362A-Y392A, CX_3CL1-LifeAct-GFP and RFP, GPI-GFP, GT-46 YFP, and the tail of K-Ras-GFP (Kenworthy *et al.*, 2004; Yeung *et al.*, 2006; Durkan *et al.*, 2007; Riedl *et al.*, 2008; Huang *et al.*, 2009; Tole *et al.*, 2010). For gene silencing, HUVECs were electroporated with siRNA directed against human ADAM10 or nontargeting, scrambled siRNA (Santa Cruz Biotechnology, Santa Cruz, CA) on days 0 and 2. Knockdown was confirmed by immunoblotting. Experiments were performed on day 4.

Antibodies and reagents
The primary antibodies used in this study included goat anti-human CX_3CL1 immunoglobulin G (IgG) and mouse anti-human ADAM10 IgG from R&D Systems (Minneapolis, MN), rabbit anti-human ADAM10 IgG (Abcam, Toronto, Canada), and rabbit anti-human caveolin-1 IgG (BD Transduction Laboratories, San Jose, CA). All fluorescent and biotin-conjugated secondary antibodies were obtained from Jackson ImmunoResearch Laboratories (Bar Harbor, ME) and include DyLight 549–conjugated donkey anti-goat IgG, Cy5-conjugated donkey anti-goat IgG, DyLight 488–conjugated donkey anti-mouse IgG, DyLight 488–conjugated donkey anti-rabbit IgG, biotin-conjugated rat anti-mouse Fab fragment, and biotin-conjugated rabbit anti-goat Fab fragment. Streptavidin Qdot 655 was obtained from Invitrogen (Burlington, Canada).

The following reagents were used: MβCD, Lat B, and Toxin B from Sigma-Aldrich (Oakville, Canada), Cal A (Calbiochem, Gibbstown, NJ), Draq5 (Biostatus, Shepshed, United Kingdom), fibronectin (Roche, Mississauga, Canada), filipin from *Streptomyces filipinensis* (Polysciences, Warrington, PA), wheat germ agglutinin (WGA; Life Technologies), TAPI-2 (Peptides International, Louisville, KY), and G1254023X (Tocris, Minneapolis, MN).

Single-particle tracking and diffusion analysis
HUVECs were grown to confluence on glass coverslips coated with fibronectin (100 µg/ml). In unstimulated conditions, these cells express a negligible amount of CX_3CL1 protein on their cell surface. HUVECs were next incubated with TNF-α (0.02 µg/ml) for 4 h to upregulate endogenous levels of cell surface CX_3CL1 (Bazan *et al.*, 1997). Cells were incubated with anti-CX_3CL1 (0.2 µg/ml) or anti-ADAM10 antibody (Ab; 0.01 µg/ml) diluted in EBM-2 for 10 min at 10°C, washed with cold Hank's balance salt solution (HBSS), and then incubated with biotinylated secondary Fab fragment (0.375 µg/ml) for 10 min at 10°C. Cells were washed further and then incubated with Qdot 655–conjugated streptavidin (0.1 nM) diluted in HBSS for 4 min at 10°C. To block unengaged streptavidin, cells were incubated with cold medium containing biotin for 20 s. After washing, the coverslip was transferred to a Leiden chamber, warmed to 37°C, and placed on the heated stage of an Axiovert 200 M inverted epifluorescence microscope (Carl Zeiss, Toronto, Canada) equipped with a custom 2.5× lens and a 100× (numerical aperture [NA] 1.45) oil-immersion objective for live-cell imaging (Jaqaman *et al.*, 2008).

SPT was performed using an Exfo X-Cite 120 light source for illumination and a Hamamatsu 9100-13 deep-cooled electron-multiplying charge-coupled device camera for recording (Hamamatsu Photonics, Bridgewater, NJ). Image acquisition was controlled using Volocity software taking 300 frame videos at a frame rate of 30 Hz. Imaged molecules of CX_3CL1 or ADAM10 were detected and tracked as described by Jaqaman *et al.* (2008). In brief, subdiffraction particle positions and intensities were estimated by 1) detecting significant local intensity maxima and 2) fitting Gaussian kernels approximating the two-dimensional point spread function of the microscope. The detected particles were tracked using a two-step single-particle tracking algorithm that could follow dense particle fields and generate complete trajectories by closing gaps and capturing merging and splitting events. Diffusion rates and diffusion types were then extracted using MSS analysis of particle displacements (Ferrari *et al.*, 2001; Ewers *et al.*, 2005; Flannagan *et al.*, 2010; Jaqaman *et al.*, 2011).

Typically, MSD{r^2} versus Δt is used to analyze a particle trajectory. For normal or free diffusion, the MSD is expected to be a linear function of time ($r^2 = 4D\Delta$). However, many molecules will exhibit a nonlinear relationship to time. The resulting anomalous diffusion can be

described as superdiffusion (directed) or subdiffusion (confined). Thus a measure of nonlinearity can be expressed by the parameter α, resulting in $r^2 = 4D\Delta t^\alpha$. This measurement can be further enhanced by a nonnegative integer ν introduced by Ferrari *et al.* (2001) such that $r^\nu \sim \Delta t^{\nu}$. The plot of $\gamma\nu$ versus ν is called the MSS, and its slope, S_{MSS}, represents a value associated with a mode of diffusion: $S_{MSS} =$ 0.5, free motion; <0.5, confined motion; >5, directed motion; 0, immobile. The S_{MSS} offers two main advantages over the MSD: 1) a smaller error in measurement due to greater linearity in the MSS and 2) a clearer distinction between modes of diffusion (Ferrari *et al.*, 2001; Ewers *et al.*, 2005; Jaqaman *et al.* 2011). For the purpose of this study, only confined and free motions were reported, as directed motion was minimal.

In parallel experiments, cells were incubated with MβCD (10 mM) for 30 min to deplete cholesterol and either Toxin B (50 ng/ml) for 105 min or Lat B (1 μM) for 10 min to disrupt actin. Cells were subsequently imaged live for SPT.

Single-molecule colocalization

HUVECs were incubated with TNF-α, and cells were fixed using 4% paraformaldehyde, blocked with 5% donkey serum for 45 min, incubated with anti-CX$_3$CL1 Ab (0.2 μg/ml) for 10 min, washed, and incubated with a Dylight 549–conjugated anti-goat Fab fragment (0.375 μg/ml) for 10 min. Cells were washed and then incubated with either anti–caveolin-1 Ab (0.036 μg/ml) for 10 min or anti-ADAM10 Ab (0.01 μg/ml) for 20 min, followed by Dylight 488–conjugated anti-rabbit (0.4 μg/ml) or anti-mouse Fab fragment (0.4 μg/ml) for 20 min. Coverslips were placed in a Leiden chamber, and single molecules were detected as described.

To investigate colocalization between CX$_3$CL1 and ADAM10, or CX$_3$CL1 and caveolin-1, the spatial relationship between the two molecules was assessed using a nearest-neighbor approach termed the SAA, as described in Heit *et al.* (2013; also see Dunne *et al.*, 2009; Lachmanovich *et al.*, 2003). Initially, the positional precision of DyLight 549 (σ_{549}) and DyLight 488 (σ_{488}) particles was calculated individually for every image, yielding values of ~30 nm. These values were then used to calculate the cross-channel positional precision (σRMS), determined by calculating the root mean square of the positional precisions for DyLight 549 and DyLight 488:

$$\sigma RMS = (\sigma_{549}^2 + \sigma_{488}^2)^{1/2}$$

To determine a CDC, the distance below which molecules are considered to be colocalized, the result of the foregoing equation was multiplied by a 90% probability cut-off (1.65 SDs), followed by the addition of the image registration accuracy of the microscope (I_{reg}):

$$CDC = 1.65\sigma RMS + I_{reg}$$

In this study, the I_{reg} was experimentally determined to be 105 nm, resulting in a CDC of 165–175 nm. Therefore a conservative CDC of ~180 nm was used for consistency in all analyses.

The Euclidean distance between each DyLight 549–labeled particle and nearest DyLight 488 particle was next measured. This method is nonsymmetrical, however, and thus all distances were measured relative to DyLight 549 (CX$_3$CL1) particles. This allowed for the coincidence of colocalization to be determined based on the fraction of DyLight 549 and 488 pairs separated by a distance ≤CDC. A Monte Carlo approach was then used to determine whether the observed colocalization differed from a randomly distributed population of particles (Metropolis and Ulam, 1949). In brief, a random population containing the same number of

observed DyLight 549 and 488 particles was generated using a uniformly distributed pseudorandom number generator. The random population was then positioned on a virtual image with the same dimensions as the observed image, and colocalization was assessed by the nearest-neighbor approach. This process was repeated 2000 times, allowing for the frequency of colocalization in a random population to be compared with the observed population.

In some instances, cells were pretreated with either a dimethyl sulfoxide (DMSO) vehicle control or the ADAM10 inhibitor G1254023X (10 μM) for 3 h, followed by treatment with Lat B (1 μM) for 10 min. Cells were then fixed and labeled for single-molecule imaging and SAA as described.

Fluorescence microscopy

To deplete cholesterol, cells were incubated with methyl-β-cyclodextrin (10 mM) for 30 min. Cholesterol content was evaluated by incubating cells with filipin (0.5 mg/ml) for 1 h using a DMIRE2 microscope equipped with 63× oil immersion objective. Detection of cell surface CX$_3$CL1 was performed using spinning-disk confocal microscopy after fixing cells in 4% paraformaldehyde, blocking with 5% donkey serum, and incubating with anti-CX$_3$CL1 Ab (0.2 μg/ml) for 1 h. Cells were washed and incubated with DyLight 549–conjugated anti-goat IgG (0.75 μg/ml) for 1 h before permeabilization with 0.1% Triton-X. Cells were then incubated with anti–caveolin-1 Ab (0.25 μg/ml) for 1 h, washed, and incubated with DyLight 488–conjugated anti-rabbit IgG (0.8 μg/ml) for 1 h.

To disrupt actin, cells were incubated with Toxin B (50 ng/ml) for 105 min or Lat B (2 μM) for 10 min. Detection of cell surface CX$_3$CL1 was performed as described.

To perturb myosin, cells were treated with blebbistatin (60 μM) for 20 min or Cal A (200 nM) for 5 min. Detection of CX$_3$CL1 in live cells was performed by spinning-disk microscopy after incubation of cells with anti-CX$_3$CL1 Ab (1 μg/ml) for 25 min at 10°C, followed by incubation with DyLight 549–conjugated anti-goat IgG (0.75 μg/ml) for 25 min at 10°C.

The spinning-disk confocal systems (Quorum Technologies, Guelph, Canada) were used with an Axiovert 200 M microscope (Carl Zeiss) equipped with 63× (NA 1.4) or 100× (NA 1.45) oil immersion objectives. These microscopes were equipped with diode-pumped solid-state lasers (440, 491, 561, 638, and 655 nm; Spectral Applied Research, Richmond Hill, Canada) and a motorized *XY* stage (Applied Scientific Instrumentation, Eugene, OR). Images were acquired using a back-thinned, electron-multiplied camera (model C9100-13 ImagEM; Hamamatsu Photonics) controlled using Velocity software, version 6.0.1 (PerkinElmer, Waltham, MA).

Membrane extractions

HUVECs were incubated with TNF-α, incubated with anti-CX$_3$CL1 Ab (1 μg/ml) for 25 min at 10°C, washed, and incubated with DyLight 549–conjugated anti-goat Fab fragment (1.5 μg/ml) for 25 min at 10°C. To label nuclei, cells were incubated with Draq5 (5 μM). Membranes were extracted in a cytoskeleton buffer containing 10 mM 2-(*N*-morpholino)ethanesulfonic acid, pH 6.1, 138 mM KCl, 3 mM MgCl$_2$, 2 mM ethylene glycol tetraacetic acid, and 0.32 M sucrose. Extractions were performed for 2 min at 4°C using 0.1% Triton X-100, and cells were fixed with 4% paraformaldehyde (Schaefer *et al.*, 2002; Medeiros *et al.*, 2006). Cells were then washed and imaged using spinning-disk confocal microscopy. The average amount of surface CX$_3$CL1 per cell was evaluated using ImageJ software (National Institutes of Health, Bethesda, MD), measuring summed fluorescence intensity through entire z-projections per field of view,

subtracting background, and dividing by the number of nuclei per field of view (Collins, 2007; Waters, 2009).

Endocytosis assays

HUVECs were treated with DMSO or Lat B for 5 min and then incubated with transferrin-488 at 37°C for 10 min (Lat B was not washed out). Cells were then placed on ice, washed with cold phosphate-buffered saline, and acid washed to removed surface-bound transferrin (Jaqaman et al., 2011). After fixation, cells were incubated with Draq5, and transferrin fluorescence was quantified by spinning-disk confocal microscopy as described. To assess CX_3CL1 internalization, HUVECs were stimulated with TNF-α and incubated with anti-CX_3CL1 Ab (1 μg/ml) for 25 min at 10°C. Cell were then stained with Draq5 and treated with latrunculin B (2 μM) or DMSO at 37°C for 15 min. For qualitative analysis, cells were fixed, and cell surface CX_3CL1 was labeled with Alexa 488–conjugated anti-goat IgG. Cells were then permeabilized, and total CX_3CL1 was labeled with a DyLight 549–conjugated secondary. For quantitative analysis, cells were fixed and labeled with a DyLight 549–conjugated anti-goat IgG (0.75 μg/ml) to label cell surface CX_3CL1 and, in parallel, permeabilized to label total CX_3CL1. CX_3CL1 fluorescence was determined for both permeabilized and nonpermeabilized conditions by spinning-disk confocal microscopy. Internalized CX_3CL1 was determined by calculating $CX_3CL1_{permeabilized} - CX_3CL1_{non-permeabilized}$ for cells incubated with LatB or DMSO.

CX_3CL1 shedding

HUVECs were incubated with TNF-α, followed by incubation with Toxin B (50 ng/ml) or Lat B (2 μM). In some experiments, cells were first incubated with the metalloprotease inhibitor TAPI-2 (20 μM) for 1 h at 37°C or electroporated with siRNA targeting ADAM10. Cells were incubated with Draq5 (5 μM) and fixed in 4% paraformaldehyde, and cell surface CX_3CL1 was immunofluorescently labeled. Soluble CX_3CL1 was detected in conditioned medium using a CX_3CL1 ELISA (R&D Systems, Minneapolis, MN), as per the manufacturer's instructions (Tole et al., 2010).

To compare shedding between full-length CX_3CL1 and truncated CX_3CL1-360, HUVECs were electroporated with the corresponding plasmids. Cells were fixed and incubated with the plasma membrane marker WGA-488. Using the free-hand tool in ImageJ, highly magnified regions of plasma membrane were delineated using WGA-488 as a reference, and the mean CX_3CL1 fluorescence per pixel was determined. After background subtraction, plasma membrane CX_3CL1 was divided by the mean total fluorescence ($CX_3CL1_{surface}/CX_3CL1_{total}$), allowing for comparison between cells of varying levels of expression (Huang et al., 2009). Soluble CX_3CL1 was measured by performing a CX_3CL1 ELISA (R&D Systems) after incubation with a DMSO vehicle control or the ADAM10 inhibitor G1254023X (10 μM) for 3 h. The absence of inhibitor was treated as the maximum amount of CX_3CL1 cleaved, and the presence of inhibitor was treated as the amount of CX_3CL1 cleaved in the absence of ADAM10. After normalization for expression levels, $CX_3CL1_{shed}/(CX_3CL1_{shed} + CX_3CL1_{cell-associated})$, these values were used to determine the fraction of chemokine specifically cleaved by ADAM10 in cells expressing full-length CX_3CL1 or truncated CX_3CL1-360.

Statistics

Statistics was performed using Prism 5 software (GraphPad, La Jolla, CA). For multiple comparisons, p values were calculated by one-way analysis of variance using Bonferroni's multiple comparison test. In all other cases, p values were calculated using Student's t test. Mathematical and statistical analyses for SPT and subdiffraction imaging experiments were performed using custom scripts written in Matlab software (MathWorks, Natick, MA; Jaqaman et al., 2008, 2011). Data are presented as mean ± SEM unless otherwise stated.

REFERENCES

Andrews NL, Lidke KA, Pfeiffer JR, Burns AR, Wilson BS, Oliver JM, Lidke DS (2008). Actin restricts FcepsilonRI diffusion and facilitates antigen-induced receptor immobilization. Nat Cell Biol 10, 955–963.

Barreiro O, Yanez-Mo M, Serrador JM, Montoya MC, Vicente-Manzanares M, Tejedor R, Furthmayr H, Sanchez-Madrid F (2002). Dynamic interaction of VCAM-1 and ICAM-1 with moesin and ezrin in a novel endothelial docking structure for adherent leukocytes. J Cell Biol 157, 1233–1245.

Bazan JF, Bacon KB, Hardiman G, Wang W, Soo K, Rossi D, Greaves DR, Zlotnik A, Schall TJ (1997). A new class of membrane-bound chemokine with a CX3C motif. Nature 385, 640–644.

Beckers CM, van Hinsbergh VW, van Nieuw Amerongen GP (2010). Driving Rho GTPase activity in endothelial cells regulates barrier integrity. Thromb Haemost 103, 40–55.

Chen Y, Veracini L, Benistant C, Jacobson K (2009). The transmembrane protein CBP plays a role in transiently anchoring small clusters of Thy-1, a GPI-anchored protein, to the cytoskeleton. J Cell Sci 122, 3966–3972.

Chiu JJ, Chien S (2011). Effects of disturbed flow on vascular endothelium: pathophysiological basis and clinical perspectives. Physiol Rev 91, 327–387.

Chung I, Akita R, Vandlen R, Toomre D, Schlessinger J, Mellman I (2010). Spatial control of EGF receptor activation by reversible dimerization on living cells. Nature 464, 783–787.

Collins TJ (2007). ImageJ for microscopy. Biotechniques 43, 25–30.

Combadiere C, Potteaux S, Gao JL, Esposito B, Casanova S, Lee EJ, Debre P, Tedgui A, Murphy PM, Mallat Z (2003). Decreased atherosclerotic lesion formation in CX3CR1/apolipoprotein E double knockout mice. Circulation 107, 1009–1016.

Cunningham KS, Gotlieb AI (2005). The role of shear stress in the pathogenesis of atherosclerosis. Lab Invest 85, 9–23.

Dreymueller D, Pruessmeyer J, Groth E, Ludwig A (2012). The role of ADAM-mediated shedding in vascular biology. Eur J Cell Biol 91, 472–485.

Dunne PD, Fernandes RA, McColl J, Yoon JW, James JR, Davis SJ, Klenerman D (2009). DySCo: quantitating associations of membrane proteins using two-color single-molecule tracking. Biophys J 97, L5–L7.

Durkan AM, Alexander RT, Liu GY, Rui M, Femia G, Robinson LA (2007). Expression and targeting of CX3CL1 (fractalkine) in renal tubular epithelial cells. J Am Soc Nephrol 18, 74–83.

Ewers H, Smith AE, Sbalzarini IF, Lilie H, Koumoutsakos P, Helenius A (2005). Single-particle tracking of murine polyoma virus-like particles on live cells and artificial membranes. Proc Natl Acad Sci USA 102, 15110–15115.

Ferrari R, Manfroi AJ, Young WR (2001). Strongly and weakly self-similar diffusion. Physica D 154, 111–137.

Flannagan RS, Harrison RE, Yip CM, Jaqaman K, Grinstein S (2010). Dynamic macrophage "probing" is required for the efficient capture of phagocytic targets. J Cell Biol 191, 1205–1218.

Fong AM, Erickson HP, Zachariah JP, Poon S, Schamberg NJ, Imai T, Patel DD (2000). Ultrastructure and function of the fractalkine mucin domain in CX(3)C chemokine domain presentation. J Biol Chem 275, 3781–3786.

Fong AM, Robinson LA, Steeber DA, Tedder TF, Yoshie O, Imai T, Patel DD (1998). Fractalkine and CX3CR1 mediate a novel mechanism of

leukocyte capture, firm adhesion, and activation under physiologic flow. J Exp Med 188, 1413–1419.

Fujita M, Takada YK, Takada Y (2012). Integrins alphavbeta3 and alpha-4beta1 act as coreceptors for fractalkine, and the integrin-binding defective mutant of fractalkine is an antagonist of CX3CR1. J Immunol 189, 5809–5819.

Fujiwara T, Ritchie K, Murakoshi H, Jacobson K, Kusumi A (2002). Phospholipids undergo hop diffusion in compartmentalized cell membrane. J Cell Biol 157, 1071–1081.

Garton KJ, Gough PJ, Blobel CP, Murphy G, Greaves DR, Dempsey PJ, Raines EW (2001). Tumor necrosis factor-alpha-converting enzyme (ADAM17) mediates the cleavage and shedding of fractalkine (CX3CL1). J Biol Chem 276, 37993–38001.

Goswami D, Gowrishankar K, Bilgrami S, Ghosh S, Raghupathy R, Chadda R, Vishwakarma R, Rao M, Mayor S (2008). Nanoclusters of GPI-anchored proteins are formed by cortical actin-driven activity. Cell 135, 1085–1097.

Gowrishankar K, Ghosh S, Saha S, C R, Mayor S, Rao M (2012). Active remodeling of cortical actin regulates spatiotemporal organization of cell surface molecules. Cell 149, 1353–1367.

Haggie PM, Kim JK, Lukacs GL, Verkman AS (2006). Tracking of quantum dot-labeled CFTR shows near immobilization by C-terminal PDZ interactions. Mol Biol Cell 17, 4937–4945.

Haskell CA, Hancock WW, Salant DJ, Gao W, Csizmadia V, Peters W, Faia K, Fituri O, Rottman JB, Charo IF (2001). Targeted deletion of CX(3)CR1 reveals a role for fractalkine in cardiac allograft rejection. J Clin Invest 108, 679–688.

Heiska L, Alfthan K, Gronholm M, Vilja P, Vaheri A, Carpen O (1998). Association of ezrin with intercellular adhesion molecule-1 and -2 (ICAM-1 and ICAM-2). Regulation by phosphatidylinositol 4, 5-bisphosphate. J Biol Chem 273, 21893–21900.

Heit B, Kim H, Cosio G, Castano D, Collins R, Lowell CA, Kain KC, Trimble WS, Grinstein S (2013). Multimolecular signaling complexes enable Syk-mediated signaling of CD36 internalization. Dev Cell 24, 372–383 .

Henson JH, Kolnik SE, Fried CA, Nazarian R, McGreevy J, Schulberg KL, Detweiler M, Trabosh VA (2003). Actin-based centripetal flow: phosphatase inhibition by calyculin-A alters flow pattern, actin organization, and actomyosin distribution. Cell Motil Cytoskeleton 56, 252–266.

Huang YW, Su P, Liu GY, Crow MR, Chaukos D, Yan H, Robinson LA (2009). Constitutive endocytosis of the chemokine CX3CL1 prevents its degradation by cell surface metalloproteases. J Biol Chem 284, 29644–29653.

Hundhausen C, Misztela D, Berkhout TA, Broadway N, Saftig P, Reiss K, Hartmann D, Fahrenholz F, Postina R, Matthews V, et al. (2003). The disintegrin-like metalloproteinase ADAM10 is involved in constitutive cleavage of CX3CL1 (fractalkine) and regulates CX3CL1-mediated cell-cell adhesion. Blood 102, 1186–1195.

Hundhausen C, Schulte A, Schulz B, Andrzejewski MG, Schwarz N, von Hundelshausen P, Winter U, Paliga K, Reiss K, Saftig P, et al. (2007). Regulated shedding of transmembrane chemokines by the disintegrin and metalloproteinase 10 facilitates detachment of adherent leukocytes. J Immunol 178, 8064–8072.

Imai T, Hieshima K, Haskell C, Baba M, Nagira M, Nishimura M, Kakizaki M, Takagi S, Nomiyama H, Schall TJ, et al. (1997). Identification and molecular characterization of fractalkine receptor CX3CR1, which mediates both leukocyte migration and adhesion. Cell 91, 521–530.

Jaqaman K, Grinstein S (2012). Regulation from within: the cytoskeleton in transmembrane signaling. Trends Cell Biol 22, 515–526.

Jaqaman K, Kuwata H, Touret N, Collins R, Trimble WS, Danuser G, Grinstein S (2011). Cytoskeletal control of CD36 diffusion promotes its receptor and signaling function. Cell 146, 593–606.

Jaqaman K, Loerke D, Mettlen M, Kuwata H, Grinstein S, Schmid SL, Danuser G (2008). Robust single-particle tracking in live-cell time-lapse sequences. Nat Methods 5, 695–702.

Jaumouille V, Farkash Y, Jaqaman K, Das R, Lowell CA, Grinstein S (2014). Actin cytoskeleton reorganization by syk regulates fcgamma receptor responsiveness by increasing its lateral mobility and clustering. Dev Cell 29, 534–546.

Just I, Fritz G, Aktories K, Giry M, Popoff MR, Boquet P, Hegenbarth S, von Eichel-Streiber C (1994). Clostridium difficile toxin B acts on the GTP-binding protein Rho. J Biol Chem 269, 10706–10712.

Kalay Z, Fujiwara TK, Kusumi A (2012). Confining domains lead to reaction bursts: reaction kinetics in the plasma membrane. PLoS One 7, e32948.

Kenworthy AK, Nichols BJ, Remmert CL, Hendrix GM, Kumar M, Zimmerberg J, Lippincott-Schwartz J (2004). Dynamics of putative raft-associated proteins at the cell surface. J Cell Biol 165, 735–746.

Kerfoot SM, Lord SE, Bell RB, Gill V, Robbins SM, Kubes P (2003). Human fractalkine mediates leukocyte adhesion but not capture under physiological shear conditions; a mechanism for selective monocyte recruitment. Eur J Immunol 33, 729–739.

Kusumi A, Ike H, Nakada C, Murase K, Fujiwara T (2005a). Single-molecule tracking of membrane molecules: plasma membrane compartmentalization and dynamic assembly of raft-philic signaling molecules. Semin Immunol 17, 3–21.

Kusumi A, Nakada C, Ritchie K, Murase K, Suzuki K, Murakoshi H, Kasai RS, Kondo J, Fujiwara T (2005b). Paradigm shift of the plasma membrane concept from the two-dimensional continuum fluid to the partitioned fluid: high-speed single-molecule tracking of membrane molecules. Annu Rev Biophys Biomol Struct 34, 351–378.

Lachmanovich E, Shvartsman DE, Malka Y, Botvin C, Henis YI, Weiss AM (2003). Co-localization analysis of complex formation among membrane proteins by computerized fluorescence microscopy: application to immunofluorescence co-patching studies. J Microsc 212, 122–131.

Lesnik P, Haskell CA, Charo IF (2003). Decreased atherosclerosis in CX3CR1-/- mice reveals a role for fractalkine in atherogenesis. J Clin Invest 111, 333–340.

Lucas AD, Bursill C, Guzik TJ, Sadowski J, Channon KM, Greaves DR (2003). Smooth muscle cells in human atherosclerotic plaques express the fractalkine receptor CX3CR1 and undergo chemotaxis to the CX3C chemokine fractalkine (CX3CL1). Circulation 108, 2498–2504.

Matthews V, Schuster B, Schutze S, Bussmeyer I, Ludwig A, Hundhausen C, Sadowski T, Saftig P, Hartmann D, Kallen KJ, et al. (2003). Cellular cholesterol depletion triggers shedding of the human interleukin-6 receptor by ADAM10 and ADAM17 (TACE). J Biol Chem 278, 38829–38839.

Mattila PK, Feest C, Depoil D, Treanor B, Montaner B, Otipoby KL, Carter R, Justement LB, Bruckbauer A, Batista FD (2013). The actin and tetraspanin networks organize receptor nanoclusters to regulate B cell receptor-mediated signaling. Immunity 38, 461–474.

Medeiros NA, Burnette DT, Forscher P (2006). Myosin II functions in actin-bundle turnover in neuronal growth cones. Nat Cell Biol 8, 215–226.

Metropolis N, Ulam S (1949). The Monte Carlo method. J Am Stat Assoc 44, 335–341.

Murai T, Maruyama Y, Mio K, Nishiyama H, Suga M, Sato C (2011). Low cholesterol triggers membrane microdomain-dependent CD44 shedding and suppresses tumor cell migration. J Biol Chem 286, 1999–2007.

Murase K, Fujiwara T, Umemura Y, Suzuki K, Iino R, Yamashita H, Saito M, Murakoshi H, Ritchie K, Kusumi A (2004). Ultrafine membrane compartments for molecular diffusion as revealed by single molecule techniques. Biophys J 86, 4075–4093.

Nakatani K, Yoshimoto S, Iwano M, Asai O, Samejima K, Sakan H, Terada M, Hasegawa H, Nose M, Saito Y (2010). Fractalkine expression and CD16+ monocyte accumulation in glomerular lesions: association with their severity and diversity in lupus models. Am J Physiol Ren Physiol 299, F207–F216.

Pelkmans L, Burli T, Zerial M, Helenius A (2004). Caveolin-stabilized membrane domains as multifunctional transport and sorting devices in endocytic membrane traffic. Cell 118, 767–780.

Prasain N, Stevens T (2009). The actin cytoskeleton in endothelial cell phenotypes. Microvasc Res 77, 53–63.

Riedl J, Crevenna AH, Kessenbrock K, Yu JH, Neukirchen D, Bista M, Bradke F, Jenne D, Holak TA, Werb Z, et al. (2008). Lifeact: a versatile marker to visualize F-actin. Nat Methods 5, 605–607.

Robinson LA, Nataraj C, Thomas DW, Howell DN, Griffiths R, Bautch V, Patel DD, Feng L, Coffman TM (2000). A role for fractalkine and its receptor (CX3CR1) in cardiac allograft rejection. J Immunol 165, 6067–6072.

Rudner DZ, Pan Q, Losick RM (2002). Evidence that subcellular localization of a bacterial membrane protein is achieved by diffusion and capture. Proc Natl Acad Sci USA 99, 8701–8706.

Ruth JH, Volin MV, Haines GK3rd, Woodruff DC, Katschke KJJr, Woods JM, Park CC, Morel JC, Koch AE (2001). Fractalkine, a novel chemokine in rheumatoid arthritis and in rat adjuvant-induced arthritis. Arthritis Rheum 44, 1568–1581.

Schaefer AW, Kabir N, Forscher P (2002). Filopodia and actin arcs guide the assembly and transport of two populations of microtubules with unique dynamic parameters in neuronal growth cones. J Cell Biol 158, 139–152.

Schulz B, Pruessmeyer J, Maretzky T, Ludwig A, Blobel CP, Saftig P, Reiss K (2008). ADAM10 regulates endothelial permeability and T-cell transmigration by proteolysis of vascular endothelial cadherin. Circ Res 102, 1192–1201.

Sinha B, Koster D, Ruez R, Gonnord P, Bastiani M, Abankwa D, Stan RV, Butler-Browne G, Vedie B, Johannes L, *et al.* (2011). Cells respond to mechanical stress by rapid disassembly of caveolae. Cell 144, 402–413.

Suzuki KG, Fujiwara TK, Sanematsu F, Iino R, Edidin M, Kusumi A (2007). GPI-anchored receptor clusters transiently recruit Lyn and G alpha for temporary cluster immobilization and Lyn activation: single-molecule tracking study 1. J Cell Biol 177, 717–730.

Thomsen P, Roepstorff K, Stahlhut M, van Deurs B (2002). Caveolae are highly immobile plasma membrane microdomains, which are not involved in constitutive endocytic trafficking. Mol Biol Cell 13, 238–250.

Ting LH, Jahn JR, Jung JI, Shuman BR, Feghhi S, Han SJ, Rodriguez ML, Sniadecki NJ (2012). Flow mechanotransduction regulates traction forces, intercellular forces, and adherens junctions. Am J Physiol Heart Circ Physiol 302, H2220–H2229.

Tole S, Durkan AM, Huang YW, Liu GY, Leung A, Jones LL, Taylor JA, Robinson LA (2010). Thromboxane prostanoid receptor stimulation induces shedding of the transmembrane chemokine CX3CL1 yet enhances CX3CL1-dependent leukocyte adhesion. Am J Physiol Cell Physiol 298, C1469–C1480.

Treanor B, Depoil D, Bruckbauer A, Batista FD (2011). Dynamic cortical actin remodeling by ERM proteins controls BCR microcluster organization and integrity. J Exp Med 208, 1055–1068.

Treanor B, Depoil D, Gonzalez-Granja A, Barral P, Weber M, Dushek O, Bruckbauer A, Batista FD (2010). The membrane skeleton controls diffusion dynamics and signaling through the B cell receptor. Immunity 32, 187–199.

Tsou CL, Haskell CA, Charo IF (2001). Tumor necrosis factor-alpha-converting enzyme mediates the inducible cleavage of fractalkine. J Biol Chem 276, 44622–44626.

Waters JC (2009). Accuracy and precision in quantitative fluorescence microscopy. J Cell Biol 185, 1135–1148.

Yeung T, Terebiznik M, Yu L, Silvius J, Abidi WM, Philips M, Levine T, Kapus A, Grinstein S (2006). Receptor activation alters inner surface potential during phagocytosis. Science 313, 347–351.